The Astrophysical Journal, 897:91 (17pp), 2020 July 1 https://doi.org/10.3847/1538-4357/ab765b

The ALMA Spectroscopic Survey in the HUDF: Deep 1.2 mm Continuum Number Counts

Jorge González-López[1,2], Mladen Novak[3], Roberto Decarli[4], Fabian Walter[3,5], Manuel Aravena[2], Chris Carilli[5,6], Leindert Boogaard[7], Gergö Popping[3,8], Axel Weiss[9], Roberto J. Assef[2], Franz Erik Bauer[10,11,12], Rychard Bouwens[7], Paulo C. Cortes[13,14], Pierre Cox[15], Emanuele Daddi[16], Elisabete da Cunha[17,18,19], Tanio Díaz-Santos[2], Rob Ivison[8,20], Benjamin Magnelli[21], Dominik Riechers[3,22,25], Ian Smail[23], Paul van der Werf[7], and Jeff Wagg[24]
[1] Las Campanas Observatory, Carnegie Institution of Washington, Casilla 601, La Serena, Chile; jgonzalez@carnegiescience.edu
[2] Núcleo de Astronomía de la Facultad de Ingeniería y Ciencias, Universidad Diego Portales, Av. Ejército Libertador 441, Santiago, Chile
[3] Max Planck Institute für Astronomie, Königstuhl 17, D-69117 Heidelberg, Germany
[4] INAF-Osservatorio di Astrofisica e Scienza dello Spazio, via Gobetti 93/3, I-40129, Bologna, Italy
[5] National Radio Astronomy Observatory, Pete V. Domenici Array Science Center, P.O. Box O, Socorro, NM 87801, USA
[6] Battcock Centre for Experimental Astrophysics, Cavendish Laboratory, Cambridge CB3 0HE, UK
[7] Leiden Observatory, Leiden University, P.O. Box 9513, NL-2300 RA Leiden, The Netherlands
[8] European Southern Observatory, Karl-Schwarzschild-Strasse 2, D-85748, Garching, Germany
[9] Max-Planck-Institut für Radioastronomie, Auf dem Hügel 69, D-53121 Bonn, Germany
[10] Instituto de Astrofísica, Facultad de Física, Pontificia Universidad Católica de Chile Av. Vicuña Mackenna 4860, 782-0436 Macul, Santiago, Chile
[11] Millennium Institute of Astrophysics (MAS), Nuncio Monseñor Sótero Sanz 100, Providencia, Santiago, Chile
[12] Space Science Institute, 4750 Walnut Street, Suite 205, Boulder, CO 80301, USA
[13] Joint ALMA Observatory—ESO, Av. Alonso de Córdova, 3104, Santiago, Chile
[14] National Radio Astronomy Observatory, 520 Edgemont Rd, Charlottesville, VA, 22903, USA
[15] Institut d'astrophysique de Paris, Sorbonne Université, CNRS, UMR 7095, 98 bis bd Arago, F-7014 Paris, France
[16] Laboratoire AIM, CEA/DSM-CNRS-Universite Paris Diderot, Irfu/Service d'Astrophysique, CEA Saclay, Orme des Merisiers, F-91191 Gif-sur-Yvette cedex, France
[17] International Centre for Radio Astronomy Research, University of Western Australia, 35 Stirling Hwy, Crawley, WA 6009, Australia
[18] Research School of Astronomy and Astrophysics, Australian National University, Canberra, ACT 2611, Australia
[19] ARC Centre of Excellence for All Sky Astrophysics in 3 Dimensions (ASTRO 3D), Australia
[20] Institute for Astronomy, University of Edinburgh, Royal Observatory, Blackford Hill, Edinburgh EH9 3HJ, UK
[21] Argelander-Institut für Astronomie, Universität Bonn, Auf dem Hügel 71, D-53121 Bonn, Germany
[22] Cornell University, 220 Space Sciences Building, Ithaca, NY 14853, USA
[23] Centre for Extragalactic Astronomy, Department of Physics, Durham University, South Road, Durham, DH1 3LE, UK
[24] SKA Organization, Lower Withington Macclesfield, Cheshire SK11 9DL, UK
Received 2019 September 27; revised 2020 February 9; accepted 2020 February 11; published 2020 July 6

Abstract

We present the results from the 1.2 mm continuum image obtained as part of the Atacama Large Millimeter/submillimeter Array Spectroscopic Survey in the Hubble Ultra Deep Field. The 1.2 mm continuum image has a size of 2.9 (4.2) arcmin^2 within a primary beam response of 50% (10%) and an rms value of 9.3 μJy beam^{-1}. We detect 35 sources at high significance (Fidelity $\geqslant$0.5); 32 have well-characterized near-infrared Hubble Space Telescope counterparts. We estimate the 1.2 mm number counts to flux levels of $<$30 μJy in two different ways: we first use the detected sources to constrain the number counts and find a significant flattening of the counts below $S_\nu \sim 0.1$ mJy. In a second approach, we constrain the number counts using a probability of deflection statistics ($P(D)$) analysis. For this latter approach, we describe new methods to accurately measure the noise in interferometric imaging (employing jackknifing in the cube and in the visibility plane). This independent measurement confirms the flattening of the number counts. Our analysis of the differential number counts shows that we are detecting $\sim$93% ($\sim$100% if we include the lower fidelity detections) of the total continuum dust emission associated with galaxies in the Hubble Ultra Deep Field. The ancillary data allow us to study the dependence of the 1.2 mm number counts on redshift ($z = 0$–4), galaxy dust mass ($M_{\rm dust} = 10^7$–$10^9 M_\odot$), stellar mass ($M_* = 10^9$–$10^{12} M_\odot$), and star formation rate (SFR $= 1 - 1000\ M_\odot\ {\rm yr}^{-1}$). In an accompanying paper we show that the number counts are crucial to constrain galaxy evolution models and the understanding of star-forming galaxies at high redshift.

Unified Astronomy Thesaurus concepts: Millimeter astronomy (1061); Surveys (1671); Galaxies (573); Infrared sources (793)

1. Introduction

In order to explain the number of stars and galaxies we see in the local universe, a large population of star-forming galaxies must have been present in the past (Madau & Dickinson 2014). The stellar radiation produced by such young galaxies will be partially absorbed by interstellar dust and re-emitted in the mid- and far-infrared. The combination of the emission of all galaxies at different times then produces a cosmic infrared background (CIB).

The *Cosmic Background Explorer* satellite detected the CIB in multiple wavelengths and concluded that the observed emission should correspond to dust-reprocessed emission from high-z galaxies (Puget et al. 1996; Fixsen et al. 1998; Hauser et al. 1998; Hauser & Dwek 2001).

Soon after the detection of the CIB, bolometer camera observations in submillimeter bands revealed a population of dust-enshrouded highly star-forming galaxies at high redshift

[25] Humboldt Research Fellow.

(Smail et al. 1997; Barger et al. 1998; Hughes et al. 1998; Eales et al. 1999). These galaxies are bright at submillimeter wavelengths and barely detected in the UV/optical bands, hence their name submillimeter galaxies or dusty star-forming galaxies (DSFGs). The discovery of this population of galaxies showed that a considerable fraction of the star formation activity in high-redshift galaxies could be obscured by dust (e.g., an early review by Blain et al. 2002).

As expected, the Atacama Large Millimeter/Submillimeter Array (ALMA) is revolutionizing the study of DSFGs. First by allowing for very high angular resolution observations of bright DSFGs (e.g., ALMA Partnership et al. 2015; Hodge et al. 2016; Iono et al. 2016; Tadaki et al. 2018) and also by allowing the detection of the faint high-redshift population (Watson et al. 2015; Laporte et al. 2017; Hashimoto et al. 2019). It is not a surprise that some of the observations made with ALMA were to follow-up single-dish submillimeter sources (e.g., Hodge et al. 2013; Karim et al. 2013; Simpson et al. 2015; Stach et al. 2018). The next step was to conduct deep ALMA surveys to search for the population of faint DSFGs. These first attempts focused on fields with deep archival data such as the Subaru/XMM-Newton Deep Survey Field (Hatsukade et al. 2013, 2016), SSA22 (Umehata et al. 2017), the GOODS-S/Hubble Ultra Deep Field (HUDF, Aravena et al. 2016; Walter et al. 2016; Dunlop et al. 2017; Franco et al. 2018; Hatsukade et al. 2018), Frontier Fields (González-López et al. 2017; Muñoz Arancibia et al. 2018), on calibrator fields (Oteo et al. 2016), and on combined multiple single-pointing fields (Ono et al. 2014; Carniani et al. 2015; Fujimoto et al. 2016; Oteo et al. 2016).

The flux density distribution of DSFGs is a powerful tool to test galaxy evolution models. Straightforward measurements, such as the galaxy number counts, are the result of several intrinsically complex processes. In order to model the observed number counts of galaxies at submillimeter and millimeter wavelengths, we need to take into account the dark matter halo distribution (e.g., Klypin et al. 2011, 2016), the star formation history and modes (e.g., Béthermin et al. 2012; Sargent et al. 2012), the spectral energy distribution (SED) of galaxies (e.g., da Cunha et al. 2013), the redshift distribution (e.g., Béthermin et al. 2015), the type of observations (e.g., Muñoz Arancibia et al. 2015; Béthermin et al. 2017), and the observed distribution of galaxies at all wavelengths (e.g., Schreiber et al. 2017). In order to test the galaxy evolution models, we need to obtain reliable number counts of well-characterized DSFGs.

In this work we present the band 6 (1.2 mm) continuum observations obtained as part of the ALMA Spectroscopic Survey in the HUDF (ASPECS, Walter et al. 2016). The HUDF, and especially the eXtreme Deep Field, is the deepest extragalactic field observed by the Hubble Space Telescope (Beckwith et al. 2006; Illingworth et al. 2013). ASPECS Large Program (ASPECS-LP) is an ALMA cycle 4 large program that represents an unparalleled 3D survey in a contiguous $\sim$4 arcmin^2 region in the HUDF designed to trace the cosmic evolution of cool gas and dust. The first results using the band 3 observations were recently published (Aravena et al. 2019; Boogaard et al. 2019; Decarli et al. 2019; González-López et al. 2019; Popping et al. 2019). By collapsing the band 6 data, we obtain a deep continuum image that can be used to search for the faint population of DSFGs (hereafter referred to as 1 mm galaxies). We present the number counts of sources detected in the deep continuum image of the HUDF and how they change for different galaxy properties.

This paper is structured as follows: in Section 2 we present the observations, the calibration, and the imaging process. In Section 3 we describe the methods used to extract the sources as well as to estimate the number counts. In Section 4 we present the results from the source extraction, and in Section 5 we discuss the implications of these results. Finally, in Section 6 we present our conclusions.

Throughout this paper, the properties of the galaxies were estimated adopting a Chabrier (2003) initial mass function and a flat ΛCDM cosmology as in Boogaard et al. (2019) and Aravena et al. (2019, 2020).

2. Observations and Data Processing

2.1. Survey Design

The data used in this work correspond to the band 6 observations from ASPECS-LP. The observational setups used in ASPECS-LP are the same as the ones used in ASPECS-Pilot observations presented in Walter et al. (2016). We used eight spectral tunings that cover most of the ALMA band 6 (212–272 GHz, $\approx$94% of band 6). The mosaic consists of 85 pointings separated by 11″ ($\approx$51% of the half-power beam width at the highest frequency setup) and is Nyquist-sampled at all frequencies. The ASPECS-LP observations were designed to obtain a sensitivity similar to that of the ASPECS-Pilot observations. The final data were deeper than requested because several of the executions were obtained with excellent weather conditions and low precipitable water vapor (pwv $<$ 1 mm).

2.2. Data Reduction, Calibration, and Imaging

We processed the data with the CASA ALMA calibration pipeline (v.5.1.1; McMullin et al. 2007), using the calibration and flagging input provided by ALMA. We created the continuum images as well as the data cubes with CASA v.5.4.0-70. This version of CASA fixed several problems that affected large mosaic imaging. We obtained the continuum images using the task TCLEAN with natural weighting and multi-frequency synthesis (mfs) mode. We created the cleaned images by placing cleaning boxes on all the sources with a signal-to-noise ratio (S/N) $\geqslant$ 5 and cleaning down to 20 μJy beam^{-1}. The deepest region of the continuum image has an rms value of 9.3 μJy beam^{-1} with a beam size of 1.″53 $\times$ 1.″08. The continuum image is shown in Figure 1. We used the same procedure to obtain a tapered image with an rms value of 11.3 μJy beam^{-1} with a beam size of 2.″37 $\times$ 2.″05. We used the tapered image to search for extended emission that could be missed by the original natural weighting image. We chose this tapered beam size because it offers additional sensitivity to slightly extended emission without significant loss of depth. The resulting beam is similar to the band 3 continuum image beam of $\approx$2.″1 (González-López et al. 2019).

In addition to the continuum image, we created the data cube covering the frequency range. We identified the spaxels of each continuum source that contained bright emission lines. We discovered several emission lines associated with the continuum-detected sources, with some sources showing up to three emission lines in band 6. Because of this, we proceeded to create a line-free continuum image by flagging all the frequency channels with strong emission lines (Decarli et al. 2019; González-López et al. 2019). We repeated the procedure

that was used for the original cleaned continuum image, resulting in an rms of 10.0 μJy beam^{-1}. This image was used to search for flux density boosting produced by the emission lines.

3. Methods

3.1. Source Search

We performed 2D source extraction using LineSeeker in the same manner as was done for the ASPECS-LP 3 mm continuum image (González-López et al. 2019). LineSeeker uses a simple algorithm to extract sources either in collapsed channel maps created for the search of emission lines or in continuum images. In both cases the extraction is based on the source peak flux density per beam. Similar extraction algorithms have been used in previous studies (Aravena et al. 2016; González-López et al. 2017). The sources were independently extracted in the natural weighting and tapered images. We estimated an initial rms value from the image, excluded all the pixels with S/N $\geqslant$ 5 from the image, and estimated a new rms value. We selected all the pixels with new S/N $\geqslant$ 2 and grouped them together using the algorithm called density-based spatial clustering of applications with noise (DBSCAN; Ester et al. 1996). DBSCAN is useful to recover the emission of extended sources as long as such emission is traced by pixels with S/N $\geqslant$ 2. At the same time, two blended sources are associated with the same source if they are connected by pixels with S/N $\geqslant$ 2. Visual inspection is needed to determine if blending occurs for any source. LineSeeker automatically estimated a fidelity value for each source in the output catalog by comparing the number of positive and negatives with similar S/Ns as

$$\mathrm{Fidelity} = 1 - \frac{N_{\mathrm{Neg}}}{N_{\mathrm{Pos}}}, \quad (1)$$

with N_{Neg} and N_{Pos} being the number of negative and positive continuum candidates detected with a given S/N value.

We estimated the completeness correction by injecting point sources of different flux density values into the *uv*-plane jackknife noise-reference image (described in Section 3.3.2). In each iteration we injected 20 point sources convolved by the corresponding clean synthesized beam. We chose to inject only 20 sources at a time to decrease the probability of blending. The process was repeated until we injected 20,000 sources. We then used LineSeeker to extract the sources from the new images. We classified each of the injected sources as recovered if they were detected with an S/N value higher than a given limit associated with a fidelity equal to 50% (S/N = 4.3 for the natural image and S/N = 3.3 for the tapered image). We used the same images to estimate the flux-boosting effect on the recovered sources. We estimate an excess of $\approx$11% in the measured flux density for the sources detected with fidelity equal to 50%. In both images the flux density excess decreased to $\lesssim$3% at S/N $\sim$ 5. The sources were injected in the image plane instead of the *uv*-plane. According to NAASC Memo #117, the flux recovery of sources in ALMA mosaic images should be reliable.

The final list of sources detected with a fidelity equal to or higher than 50% in the natural weighted or the tapered images is presented in Table 1. The position of the sources and the PB levels are shown in Figure 2. For the sources detected in both images, the fidelity value was selected as the highest of the two. In order to account for possible extended faint galaxies, all completeness correction values were taken from the tapered image analysis. As reference, we detect 27 positive sources with S/N $\geqslant$ 4.3 and 2 negative sources with the same S/N in the natural weighted image. In the case of the tapered image we detect 32 positive sources with S/N $\geqslant$ 3.3 and 3 negative sources.

3.2. Direct Number Counts

The most common method for estimating the number counts is to directly count the detected sources and correct for the fidelity and completeness. We followed the recipe that was used by Aravena et al. (2016) and González-López et al. (2019), where the number counts per bin ($N(S_i)$) are computed as

$$N(S_i) = \frac{1}{A}\sum_{j=1}^{x_j}\frac{P_j}{C_j}, \quad (2)$$

where A is the total area of the observations (1.16×10^{-3} deg^2 for PB $\geqslant$ 0.1), P_j is the probability of each source being real (Fidelity), and C_j is the completeness correction for the corresponding intrinsic flux density. Note that we estimated the completeness correction on the mosaic primary beam corrected plane, so the information about the different sensitivity across the map is included in this correction factor and not in an associated effective area per source. To account for extended emission that is missed by the natural weighting image, we used the correction factor estimates from the tapered image for all sources. These correction factors are $\approx$1.3–1.4$\times$ larger in the faint end (30–40 μJy) and practically equal for sources brighter than 0.1 mJy. The flux density values for all the sources are corrected by flux-boosting effects (described in Section 3.1) at the moment of estimating the number counts.

We obtained the cumulative number counts by summing each $N(S_i)$ over all the possible $\geqslant S_i$. The size of the bins is $\log S_\nu = 0.25$ for the differential number counts and $\log S_\nu = 0.1$ for the cumulative number counts. We used all source candidates with Fidelity $\geqslant$0.5 listed in Table 1 for the number counts. The error estimates for the number counts were calculated by combining Poisson statistics errors based on the number of sources per bin and the intrinsic uncertainty of the flux density measurements. For the latter we generated new flux density values for each source following a Gaussian distribution given by the corresponding flux density estimates and their errors. We then measured the number counts using these new flux density values. We repeated this process 1,000 times and measured the scatter per bin. For simplicity, this scatter is added in quadrature to the Poisson statistics errors. We checked that the main results from the direct number counts did not change when we applied a more restrictive cut in PB. We repeated the analysis using PB $\geqslant$ 0.5 and PB $\geqslant$ 0.9 (the latter corresponding to approximately half of the total area), and the number counts in the faint end remained the same. The only difference appears in the bright end where the error bars increase because the area we used is smaller.

Table 1
Continuum Source Candidates in the ASPECS-LP 1.2 mm Continuum Image

ID ASPECS-LP.1 mm. (1)	R.A. (2)	Decl. (3)	S/N (4)	Fidelity (5)	PBC (6)	$S_{1.2\,mm}$ (μJy) (7)	*HST*? (8)
C01	03:32:38.54	−27:46:34.60	67.6	$1.0^{+0.0}_{-0.0}$	0.97	752.0 ± 24.2	Yes
C02	03:32:36.96	−27:47:27.20	44.1	$1.0^{+0.0}_{-0.0}$	0.99	431.6 ± 9.8	Yes
C03	03:32:34.43	−27:46:59.79	30.7	$1.0^{+0.0}_{-0.0}$	0.86	429.2 ± 23.0	Yes
C04	03:32:41.02	−27:46:31.60	26.8	$1.0^{+0.0}_{-0.0}$	0.82	316.2 ± 11.8	Yes
C05	03:32:39.75	−27:46:11.60	23.2	$1.0^{+0.0}_{-0.0}$	0.66	461.2 ± 28.2	Yes
C06	03:32:43.53	−27:46:39.19	22.6	$1.0^{+0.0}_{-0.0}$	0.2	1071.0 ± 47.4	Yes
C07	03:32:35.08	−27:46:47.80	20.1	$1.0^{+0.0}_{-0.0}$	0.84	232.6 ± 11.5	Yes
C08	03:32:38.03	−27:46:26.60	16.2	$1.0^{+0.0}_{-0.0}$	0.96	163.2 ± 10.1	Yes
C09	03:32:35.56	−27:47:04.20	15.9	$1.0^{+0.0}_{-0.0}$	1.0	154.6 ± 9.7	Yes
C10	03:32:40.07	−27:47:55.80	13.8	$1.0^{+0.0}_{-0.0}$	0.49	342.1 ± 33.8	Yes
C11	03:32:43.32	−27:46:46.99	13.6	$1.0^{+0.0}_{-0.0}$	0.46	288.8 ± 21.2	Yes
C12	03:32:36.48	−27:46:31.80	10.7	$1.0^{+0.0}_{-0.0}$	0.91	113.7 ± 10.6	Yes
C13	03:32:42.99	−27:46:50.19	9.7	$1.0^{+0.0}_{-0.0}$	0.66	116.0 ± 15.6	Yes
C14a	03:32:41.69	−27:46:55.80	9.4	$1.0^{+0.0}_{-0.0}$	0.95	95.9 ± 9.8	Yes
C14b	03:32:41.85	−27:46:57.00	9.4	$1.0^{+0.0}_{-0.0}$	0.95	89.2 ± 19.7	Yes
C15	03:32:42.37	−27:47:08.00	8.9	$1.0^{+0.0}_{-0.0}$	0.73	118.0 ± 13.2	Yes
C16	03:32:39.87	−27:47:15.20	8.8	$1.0^{+0.0}_{-0.0}$	0.98	142.8 ± 17.6	Yes
C17	03:32:38.80	−27:47:14.80	8.1	$1.0^{+0.0}_{-0.0}$	0.99	96.9 ± 15.3	Yes
C18	03:32:37.37	−27:46:45.80	7.2	$1.0^{+0.0}_{-0.0}$	0.98	107.2 ± 16.1	Yes
C19	03:32:36.19	−27:46:28.00	6.8	$1.0^{+0.0}_{-0.0}$	0.78	84.6 ± 12.4	Yes
C20	03:32:35.77	−27:46:27.60	6.0	$1.0^{+0.0}_{-0.0}$	0.62	94.5 ± 15.7	Yes
C21	03:32:36.00	−27:47:25.80	5.5	$1.0^{+0.0}_{-0.0}$	0.92	58.3 ± 10.5	Yes
C22	03:32:37.61	−27:47:44.20	5.5	$1.0^{+0.0}_{-0.0}$	0.91	58.8 ± 10.7	Yes
C23	03:32:35.55	−27:46:26.20	5.4	$1.0^{+0.0}_{-0.0}$	0.48	147.5 ± 29.8	Yes
C24	03:32:38.77	−27:48:10.40	5.4	$1.0^{+0.0}_{-0.0}$	0.39	134.5 ± 24.9	Yes
C25	03:32:34.87	−27:46:40.80	5.4	$1.0^{+0.0}_{-0.0}$	0.58	90.0 ± 16.8	Yes
C26	03:32:34.70	−27:46:45.00	4.3	$0.54^{+0.17}_{-0.17}$	0.64	65.3 ± 15.2	Yes
C27	03:32:40.22	−27:47:38.20	4.1	$0.78^{+0.08}_{-0.08}$	0.85	46.4 ± 11.3	No
C28	03:32:40.84	−27:46:16.80	3.9	$0.87^{+0.02}_{-0.03}$	0.44	184.1 ± 45.8	Yes
C29	03:32:34.45	−27:47:35.60	3.5	$0.8^{+0.04}_{-0.04}$	0.13	307.8 ± 75.3	No
C30	03:32:38.79	−27:47:32.60	3.5	$0.8^{+0.04}_{-0.04}$	1.0	34.1 ± 9.7	Yes
C31	03:32:37.07	−27:46:17.40	3.5	$0.8^{+0.04}_{-0.04}$	0.84	47.4 ± 11.5	Yes
C32	03:32:37.73	−27:47:06.80	3.5	$0.8^{+0.04}_{-0.04}$	0.99	40.5 ± 9.8	Yes
C33	03:32:38.51	−27:47:02.80	3.3	$0.55^{+0.1}_{-0.09}$	0.98	41.8 ± 9.8	Yes
C34	03:32:40.04	−27:46:26.40	3.3	$0.55^{+0.1}_{-0.09}$	0.91	38.7 ± 10.7	No

Note. (1) Identification for continuum source candidates discovered in the ASPECS-LP 1.2 mm continuum image. (2) R.A. (J2000). (3) decl. (J2000). (4) S/N value obtained by LineSeeker assuming an unresolved source. (5) Fidelity estimate using negative detection and Poisson statistics. (6) Mosaic primary beam response. (7) Integrated flux density at 1.2 mm obtained after removing the channels with bright emission lines when necessary. (8) Presence of *HST* counterpart. Details in Aravena et al. (2020).

3.3. Number Counts

3.3.1. Input Needed for Analysis

An alternative method for estimating the intrinsic distribution of sources in the observed data is to compare the observed image pixel distribution to what would be produced by a given assumed number counts distribution. This is called probability of deflection statistics, or $P(D)$ analysis (Condon 1974) ,and has been used to estimate the number counts from noise-confused bolometer camera observations (e.g., Hughes et al. 1998; Weißet al. 2009).

To perform this $P(D)$ analysis, or forward modeling, we needed to know the dirty beam, the mosaic primary beam response, and the intrinsic noise properties of the observations. We produced the first two maps with TCLEAN at the imaging stage. The one missing piece was the intrinsic noise properties of the observations. We could not use the residual map created by TCLEAN as noise reference because it can be contaminated by sources that are not bright enough to be selected for cleaning boxes and by confusion noise (Condon 1974; Scheuer 1974). We needed a method to remove all the real signal emission from the observations.

3.3.2. Noise Reference Images

We here present two independent approaches to obtain a noise-reference image from a calibrated ALMA data set. The first is based on the jackknife resampling used in single-dish bolometer observations (Perera et al. 2008; Scott et al. 2008; Weißet al. 2009). If the emission is stable with time, then all the

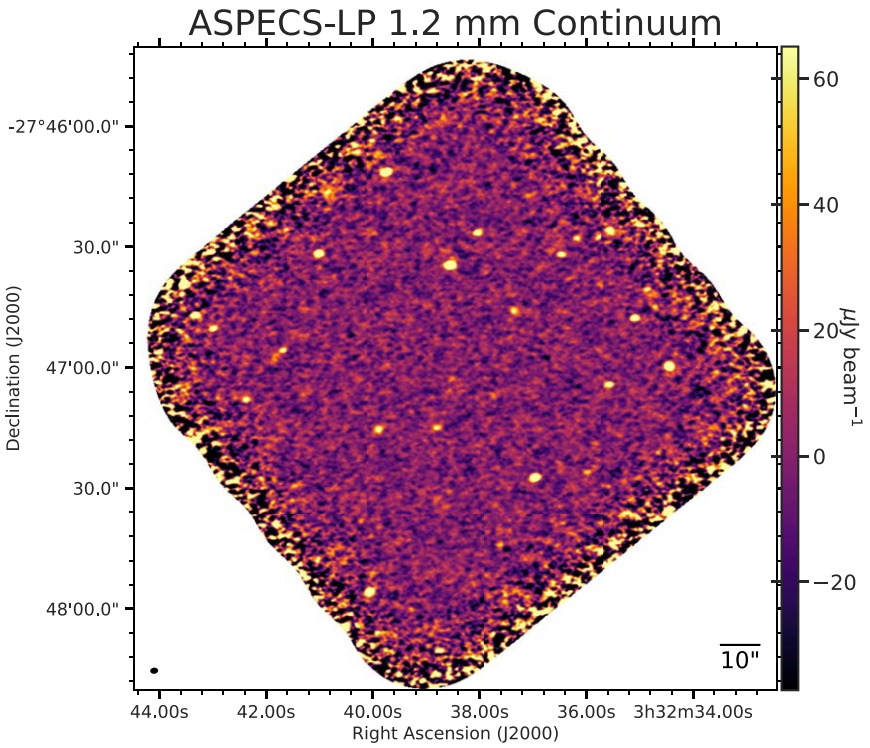

Figure 1. 1.2 mm continuum image in the H–UDF obtained as part of ASPECS-LP. The image is obtained using natural weighting, and it is corrected for the mosaic primary beam response. The total area shown here corresponds to 4.2 arcmin^2 (PB $\geqslant$ 0.1). The synthesized beam is shown in the bottom left corner.

real emission is removed from the image produced by the combination of the jackknifed scans (where the amplitudes in every second scan are multiplied by -1), whereas the noise properties are conserved. This will provide a good representation of the noise properties of the observations. This jackknife resampling cannot be used with interferometric observations because different scans do not provide information from the same region on the sky. Each interferometric integration corresponds to one point in the *uv*-plane and is sensitive to one determined position and angular scale on the sky. To bypass this limitation, we jackknifed the observations by inverting (multiplying the real and imaginary part by -1 or shifting the phase by 180°) every second visibility, which artificially creates destructive interference on the real sky emission.

The second approach to obtain a noise-reference image is also based on jackknife resampling, but is performed in the channel space of the data cube. In a sense, all continuum images made from ALMA observations are made by combining the information from multiple channels into one. Such combination can be made by fitting a continuum emission to all different channels, as is done by TCLEAN in mfs mode, or by collapsing the associated data cube. Based on this, we randomly inverted (multiplied by -1) half of the channels in the dirty cube created for the band 6 ASPECS-LP data. We repeated this process 100 times in order to obtain several realizations of the noise. For each jackknifed dirty cube, we created a continuum noise image by taking the weighted average of all channels. We calculated the weights by channels as $w = 1/\sigma_i^2$, with σ_i being the rms of each individual channel. This weight scheme should be similar to the continuum image produced by TCLEAN in mfs mode, which uses the weights calculated during calibration and renormalized during the concatenation of the different executions.

In Figure 3 we present the histograms of the *uv*-plane noise reference and the one- and two-sigma distributions from the channel jackknife resampling. Both independent jackknife processes return very similar distributions. The rms measured in the *uv*-plane noise is 9.21 μJy beam^{-1} and the median and one-sigma range for rms values from the channel jackknifing images is $9.03^{+0.04}_{-0.03}$ μJy beam^{-1}. Based on these results, we can be confident that the real noise distribution of our data is in the range 9.0–9.2 μJy beam^{-1}. As reference, when weights of $w = 1/\sigma_i$ are used for the weighted average on the continuum image creation, the resulting rms values from the channel jackknife is 9.16 ± 0.06 μJy beam^{-1}, in agreement with the rms value obtained from the *uv*-plane noise. We conclude that the differences produced by the different weighting schemes are in the sub-μJy range.

With the dirty beam, the mosaic primary beam response, and the intrinsic noise properties of the observations, we proceeded to conduct the forward modeling of the number counts from the observed data.

3.3.3. P(D) Analysis

For the fitting process we assumed that the differential number counts can be well described by a double power-law function (Scott et al. 2002; Franco et al. 2018), as given by

$$\frac{dN}{dS} = \frac{N_0}{S_0}\left[\left(\frac{S}{S_0}\right)^{\alpha} + \left(\frac{S}{S_0}\right)^{\beta}\right]^{-1}, \quad (3)$$

with the explored ranges for the different parameters being $N_0 = (1\text{–}100) \times 10^3$ mJy^{-1}deg^{-2}, $S_0 = 0.05\text{–}1.0$ mJy, and $\alpha = 1.5\text{–}5$ and β between -2 and $+2$. Previous studies have used this double power-law function to model the number counts break seen at ~4–5 mJy at 870 μm and 1.1 m

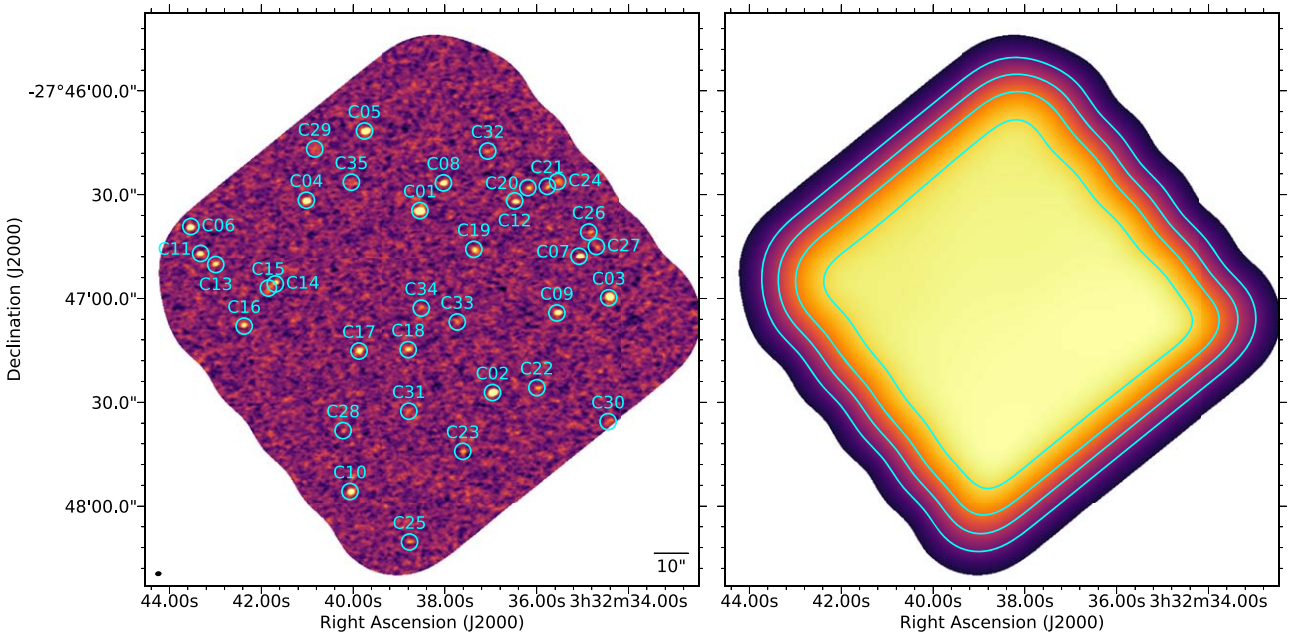

Figure 2. The left panel shows the continuum image without mosaic primary beam correction. Cyan circles show the positions and IDs of the source candidates we found to be significant. The right panel shows the primary beam response of the continuum image mosaic. The contours show where the primary beam response is 0.3, 0.5, 0.7, and 0.9. The total image has a size of 4.2 arcmin^2, while the areas within the PB $\geqslant$ 0.3, 0.5, 0.7, and 0.9 are 3.4, 2.9, 2.4, and 1.8 arcmin^2, respectively.

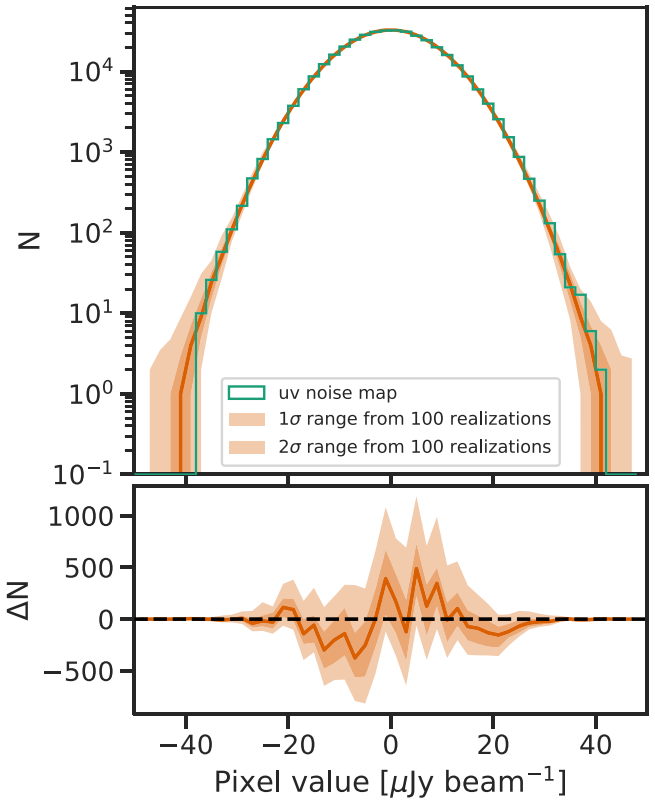

Figure 3. Top panel: comparison of the pixel distribution of the noise image created from the *uv*-plane jackknife and the dirty cube jackknife (for details, see Section 3.3). Bottom panel: residual between the *uv*-plane jackknife and the dirty cube jackknife.

(Franco et al. 2018; Stach et al. 2018). Given the area and depth of our observations, we expect to detected sources with flux density values <1 mJy. In this regime the number counts have been observed to follow a single power-law (Fujimoto et al. 2016; Franco et al. 2018). The chosen parameter space is designed to test if the single power-law function is a good description of the number counts at the faint end probed in our observations or if another break is needed.

For a given set of parameters (sampled from a grid of parameters) for the differential number counts and the area of the image, we created a list of flux density values between 0.03 and 2 mJy following this distribution. We injected point sources with the corresponding flux density value into a blank image at random positions. We then corrected the flux density for each source by the mosaic primary beam response at the corresponding position. After all the sources were injected, the blank image was convolved with the dirty beam and added to the noise-reference image.

This process was repeated 1,000 times to obtain the pixel distribution of noise plus injected sources for a given combination of parameters. We compared the different iteration distributions with the pixel histogram obtained of the real dirty image with bins of 4.3 μJy beam^{-1} and calculated the likelihood of that model being a good representation of the data, using

$$L = \prod_{i=1}^{N\mathrm{bins}} \sum_{m=0}^{M} m^{N_i} \frac{\mathrm{e}^{-m}}{N_i!} P_i(m), \quad (4)$$

with Nbins being the number of bins in the histogram, N_i is the number of pixels in each bin for the real dirty image, m is the expected number of pixels in each bin for a given combination of parameters, and $P_i(m)$ is the probability density distribution of obtaining the value m in the iterations. The likelihood is the product of the Poisson probability of measuring the observed number of pixels per bin given an expected rate m, which follows the distribution from the 1,000 iterations.

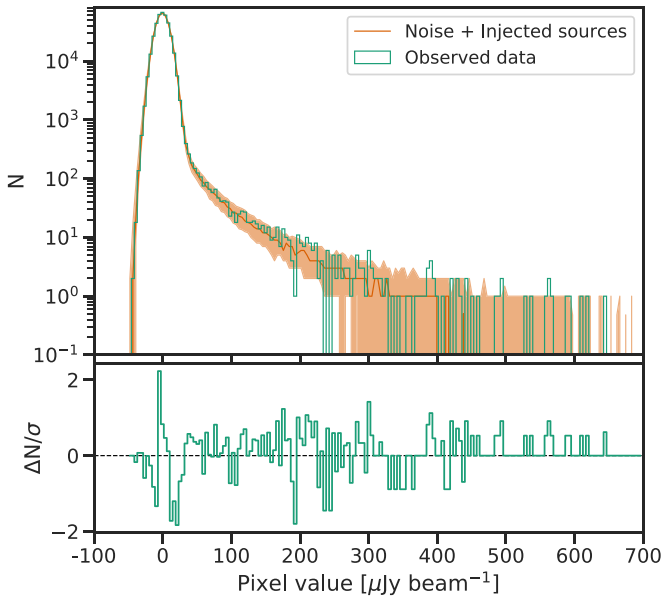

Figure 4. Top panel: the green histogram shows the pixel distribution in the natural images without primary beam correction. The orange line and region show the median distribution of pixels obtained from combining the *uv*-plane noise and injected sources following the best-fit distribution (see details in Section 3.3). Bottom panel: residual between the data and the best fit shown in red in the top panel.

For simplicity, instead of maximizing L, we minimized the associated quantity given by

$$C = -2 \ln L, \tag{5}$$

which is the maximum-likelihood-based statistic for Poisson data with a prior for the expected rate (Cash 1979).

In Figure 4 we show the observed pixel distribution (from the dirty image) compared to the best fit from the forward-modeling number counts. In the bottom panel we show the residuals of the subtraction of the best model from the observed histogram. The σ value used in the residuals was obtained by combining in quadrature the Poisson statistical errors associated with the observed number of pixels within a bin and the central 68% range of the distribution of values from the 1,000 repetitions of the injection of sources ($P(m)$). The scatter associated with the 1,000 repetitions dominates the Poisson statistical error. This is because a given source falling in a region with different mosaic primary beam values will result in a different pixel distribution.

We fit the number counts with the dirty image instead of the cleaned image. By doing so we included the effects of the dirty beam negative sidelobes on the negative pixels distribution. The complete distribution of pixels is broadened by the negative sidelobes of the dirty beam and the confusion noise (Weißet al. 2009).

4. Results

Table 1 presents the 35 high-fidelity sources found in the 1.2 mm continuum images. Only one source is barely detected in the natural image and detected with a higher S/N ratio in the tapered image. The source is ASPECS-LP-1 mm.C28, a very extended (optical effective radius $r_e > 1''$) spiral galaxy at $z = 0.622$. Visual inspection revealed that the source ASPECS-LP-1 mm.C14 corresponded to what appears to be two galaxies that are situated close to each other. MUSE and ALMA CO spectroscopy revealed that both galaxies are at similar redshift $z = 1.996$ and $z = 1.999$, indicating a possibly interacting system. Because the two near-IR (NIR) galaxies can clearly be separated (separation of $\sim 3''$ between centroids), ASPECS-LP-1 mm.C14 was cataloged as two independent sources called ASPECS-LP-1 mm.C14a and ASPECS-LP-1 mm.C14b, for the northwest and southeast galaxy, correspondingly.

Out of the 35 independent sources, 32 have clear NIR counterparts with measured spectroscopic redshifts. We define a counterpart as any bright NIR galaxy ($m_{\rm F160W} \leqslant 27$) that is located within the synthesized beam of the natural or tapered image. We stress that out of the 35 source candidates, 26 are cataloged as secure based on the fidelity values. The remaining 9 sources are cataloged as candidates based on their fidelity value alone. Despite the latter, the detection of a bright NIR counterpart increases their probability of being a real detection. Based on the measured F160W magnitudes, colors, and offsets, we estimate that up to one of the source candidates with NIR counterparts could correspond to a false association. From the Fidelity values found by LineSeeker, we expect $\sim$2.5 sources to be false. This number is remarkably similar to the number of sources without an NIR counterpart, which would suggest that these sources could indeed be false detections. We based this on the fact that our flux density values at 1 mm are at least one order of magnitude lower than the archetypal dark galaxy HDF850.1 (Walter et al. 2012) and that dust obscuration is mainly associated with massive galaxies (Whitaker et al. 2017). It is therefore expected that galaxies that are obscured enough to not be detected in the deep HUDF images should be bright at 1.2mm. Despite this, recent dark galaxies have been discovered with expected 1 mm flux density values similar to ASPECS-LP-1 mm.C29 (Simpson et al. 2014; Wang et al. 2019; Williams et al. 2019). We cannot discard that the three sources without NIR counterparts are real, but the low significance of the detections and their nondetection in deep NIR imaging make them good candidates to be false detections. The characterization of the NIR counterpart galaxies of the sources presented here is discussed in a companion paper, Aravena et al. (2020). We used the Multi-wavelength Analysis of Galaxy Physical Properties (MAGPHYS, da Cunha et al. 2008, 2015) to estimate galaxy properties such as stellar mass, dust mass, and star formation rate (SFR).

In Table 1 we also present the flux density values estimated for all the detected sources. We measured the flux densities in the same way as for the ASPECS-LP 3 mm continuum image in González-López et al. (2019). We corrected the flux density measurements for any extended emission detected in the tapered image (see the discussion in Section 3.1) and flux boosting by emission lines (of $\approx$30 μJy in the worst case). In the case of ASPECS-LP-1 mm.C14, we used different apertures to estimate the flux density and corresponding uncertainties associated with each component.

5. Discussion

5.1. Number Counts

The results from the direct sources number counts as well as the $P(D)$ analysis are presented in Figure 5. The top panels present the uncorrected and corrected number counts (blue and black points, respectively) together with the 1σ range estimated from the forward-modeling fitting. The best-fit differential number counts and the double power-law fit to the cumulative number counts resulting from the forward-modeling fitting are

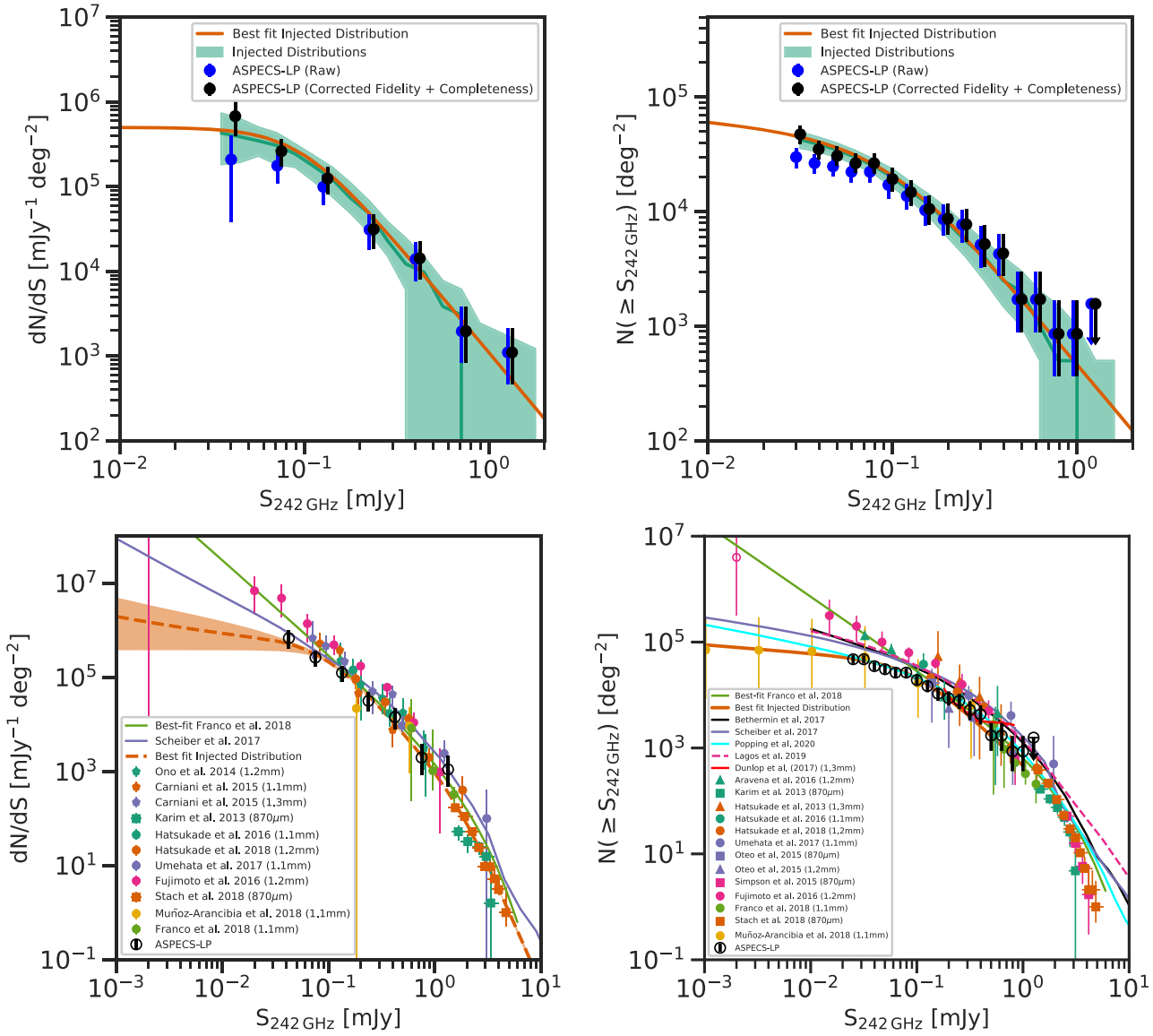

Figure 5. The top panels show the number counts (left: differential, and right: cumulative) estimates from the direct method (black data points), uncorrected (blue data points), and from the $P(D)$ analysis (green shaded regions) shown in Figure 4. The bottom panels show a comparison to previous studies and models (references in the text). The orange lines (dashed and solid) show the best-fit differential counts from the $P(D)$ analysis. Both panels show that our results agree well with previous studies at $S_\nu > 0.1$ mJy, but show a clear flattening of the counts (most visible in the cumulative number counts) at $S_\nu < 0.1$ mJy. The flattening is produced by the change in slope in the differential counts, as shown for the orange dashed line.

Table 2
Double Power-Law Fit Results Obtained from the $P(D)$ Analysis

N_0	S_0 (mJy)	α	β
(1)	(2)	(3)	(4)
	Differential number counts		
$(4.4 \pm 0.6) \times 10^4$ mJy^{-1}deg^{-2}	0.10 ± 0.02	$2.5^{+0.2}_{-0.1}$	$0.0^{+0.6}_{-0.2}$
	Cumulative number counts		
$(4.1 \pm 0.1) \times 10^3$ deg^{-2}	0.09 ± 0.02	1.94 ± 0.14	0.16 ± 0.14

presented in Table 2. The best fit is found by the distribution that minimizes C, and the 1σ range is obtained from the probability distributions obtained from the corresponding likelihood values.

Although the number counts obtained from the $P(D)$ analysis are less well constrained (because of the random positions and corresponding correction by the mosaic PB), the results from the two independent methods show excellent agreement. Importantly, the change in slope in the number counts at $S_0 \sim 0.1$ mJy in the differential and cumulative number counts is seen in both analyses. The values for the direct number counts are presented in Tables 3 and 4.

Table 3
ASPECS-LP 1.2 mm Differential Number Counts

S_ν range ($\times 10^{-3}$ mJy) (1)	$\log S_\nu$ (mJy) (2)	$N(S_\nu)$ (3)	dN/dS (mJy^{-1} deg^{-2}) (4)	$\Delta(dN/dS)_{\rm Neg}$ (mJy^{-1} deg^{-2}) (5)	$\Delta(dN/dS)^{\rm Pos}$ (mJy^{-1} deg^{-2}) (6)
31.6–56.2	−1.38	6	680,000	280,000	340,000
56.2–100.0	−1.12	9	262,000	88,000	105,000
100.0–177.8	−0.88	9	124,000	44,000	47,000
177.8–316.2	−0.62	5	31,000	13,000	16,000
316.2–562.3	−0.38	4	14,200	6300	8400
562.3–1000.0	−0.12	1	2000	1100	1900
1000.0–1778.3	0.12	1	1100	640	1060

Note. (1) Flux density bin. (2) Flux density bin center. (3) Number of sources per bin (before fidelity and completeness correction). In the case of no sources, an upper limit of <1.83 (1σ Poisson upper limit for no detection) is used. (4) Differential number count of sources per square degree. In the case of no sources, a 1σ upper limit is used. (5) Lower uncertainty in the number counts including Poisson errors and flux density errors added in quadrature. (6) Upper uncertainty in the number counts including Poisson errors and flux density errors added in quadrature.

In the bottom panels of Figure 5 we show the direct number counts, estimated as part of this work, and compared to other interferometric studies. The differential number counts are shown in the bottom left panel. To convert the results from previous studies that were conducted at different wavelengths, we used a modified blackbody and took into account the effects of the cosmic microwave background (CMB) following the recipe presented by da Cunha et al. (2013). For the dust emissivity index we used a range of $\beta = 1.5$–2.0 (Dunne & Eales 2001; Chapin et al. 2009; Clements et al. 2010; Draine 2011; Planck Collaboration et al. 2011a, 2011b), for the dust temperature we took a range of 25–40 K (Magdis et al. 2012; Magnelli et al. 2014; Schreiber et al. 2018), and we used a reference redshift of $z = 2$. The correction factor was defined as $S_{1.2\,\rm mm} = S_\lambda / K_\lambda$. The values used are $K_{1.3\,\rm mm} = 0.95$, $K_{1.1\,\rm mm} = 1.3$ and $K_{870\,\mu\rm m} = 2.9 \pm 0.5$. These factors correspond to the average of the extreme values obtained for the different properties. The correction factor for the 870 μm has a larger uncertainty given the difference in wavelengths and the intrinsic effects by the range in temperatures. The studies at 870 μm correspond to follow-up campaigns of single-dish detected sources and from calibration deep fields (Karim et al. 2013; Simpson et al. 2015; Oteo et al. 2016; Stach et al. 2018). These studies mainly sample the bright end of the 1 mm galaxy population and correspond to a flux density range of $S_\nu > 1$ mJy. The studies at 1.1–1.3 millimeters correspond to deep fields and large mosaics in blank and lensing fields (Hatsukade et al. 2013, 2016; Aravena et al. 2016; Dunlop et al. 2017; Umehata et al. 2017; Franco et al. 2018; Hatsukade et al. 2018; Muñoz Arancibia et al. 2018) as well as to the combination of multiple targeted fields (Ono et al. 2014; Carniani et al. 2015; Fujimoto et al. 2016; Oteo et al. 2016). Our results are in agreement with the results from other studies at $S_\nu > 0.1$ mJy but are lower than the rest at fainter flux density values. Our differential number count distribution has a break at $S_\nu \sim 0.1$ mJy, with the slope toward the faint end being $\beta < 0.5$. The orange dashed line shows the best fit obtained as part of the $P(D)$ analysis combined with the extrapolation toward brighter sources. The orange region shows the 1σ range obtained from the $P(D)$ analysis.

In the bottom right panel of Figure 5 we compare our cumulative number counts with other studies. Compared to most of other studies and taking into account the scatter between studies, our cumulative number counts in the range 0.1–1 mJy follows the same shape. For the counts $S < 0.1$ mJy, our results are considerably below the results from Fujimoto et al. (2016). We speculate that the difference can be explained by uncertainties in the magnification factors for some of the detections or the usage of targeted fields tracing overdense regions. In the case of the number counts from Aravena et al. (2016), we reprocessed the same images with the new methods and obtained results consistent with our new results within the error bars. The excess in the counts measured in the ASPECS-Pilot can be attributed to cosmic variance and the different methods used.

The only other cumulative number counts that seem to agree with our results come from the observations of the ALMA

Table 4
ASPECS-LP 1.2 mm Cumulative Number Counts

S_ν range ($\times 10^{-3}$ mJy) (1)	$\log S_\nu$ (mJy) (2)	$N(S_\nu)$ (3)	$N(\geqslant S_\nu)$ (deg^{-2}) (4)	$\delta N_{\rm Neg}$ (deg^{-2}) (5)	$\delta N^{\rm Pos}$ (deg^{-2}) (6)
31.6–39.8	−1.45	4	47,400	8200	8900
39.8–50.1	−1.35	2	35,100	6200	6900
50.1–63.1	−1.25	3	30,700	5500	6200
63.1–79.4	−1.15	0	26,500	4900	5600
79.4–100.0	−1.05	6	26,500	5100	5600
100.0–125.9	−0.95	4	19,300	4400	4700
125.9–158.5	−0.85	4	14,800	3500	4000
158.5–199.5	−0.75	2	10,600	2900	3400
199.5–251.2	−0.65	1	8700	2400	3000
251.2–316.2	−0.55	3	7800	2300	2700
316.2–398.1	−0.45	1	5200	1900	2400
398.1–501.2	−0.35	3	4300	1600	2100
501.2–631.0	−0.25	0	1720	840	1250
631.0–794.3	−0.15	1	1720	840	1250
794.3–1000.0	−0.05	0	860	490	820
1000.0–1258.9	0.05	1	860	490	820
1258.9–1584.9	0.15	0	<1600	…	…

Note. (1) Flux density bin. (2) Flux density bin center. (3) Number of sources per bin (before fidelity and completeness correction). In the case of no sources, an upper limit of <1.83 (1σ Poisson upper limit for no detection) is used. (4) Cumulative number count of sources per square degree. In the case of no sources, a 1σ upper limit is used. (5) Lower uncertainty in the number counts including Poisson errors and flux density errors added in quadrature. (6) Upper uncertainty in the number counts including Poisson errors and flux density errors added in quadrature.

Hubble Frontier Fields survey (Muñoz Arancibia et al. 2018). In Figure 5 we show the updated values using the five galaxy clusters. The Frontier Fields correspond to six galaxy cluster fields observed with multiple observatories with the objective of finding high-redshift galaxies (Lotz et al. 2017). These fields also have the best magnification models ever obtained for galaxy clusters (Bouwens et al. 2017; Meneghetti et al. 2017; Priewe et al. 2017). Muñoz Arancibia et al. (2018) used a detailed analysis of the source plane reconstruction of the observed images to take into account the effects introduced by the intrinsic sizes of the galaxies and the different lens models used. The results from Muñoz Arancibia et al. (2018) have large error bars associated with the intrinsic scatter introduced by the different magnification map models. Despite this, their results fully support our number count estimates.

Figure 5 also presents the 1.2 mm number counts as predicted by different galaxy evolution models (Béthermin et al. 2017; Schreiber et al. 2017; Lagos et al. 2019; Popping et al. 2020). The four models predict a flattening of the number counts below $S_\nu \sim 0.1$ mJy with different scaling factors.

In summary, our results clearly show a flattening of the cumulative number counts that is produced by the knee of the differential number counts at $S_\nu \sim 0.1$ mJy.

5.2. Number Counts for Different Populations

In order to understand the contribution of different galaxy populations to the number counts and thus to the extragalactic background light (EBL) at 1.2 mm, we split the detected sample of dust galaxies into different ranges in stellar mass, SFR, dust mass, and redshift using the best SED parameters from the associated optical/NIR counterparts (details in Aravena et al. 2020).

In Figure 6 we present the number counts for the different populations, split into redshift, dust mass, stellar mass, and SFR for the top left, top right, bottom left, and bottom right panels, respectively. With this information in hand, we can for the first time investigate how different galaxy populations contribute to the number counts. We also show in Figure 6 the corresponding number count predictions by Popping et al. (2020).

The error bars for the number counts of the different populations are estimated in a similar way as for the whole sample (see Section 3.2) with the addition of the scatter associated with the estimated properties of the galaxies. We estimate the scatter associated with the uncertainties of the galaxy properties in the same way as for the flux density values. We generate several instances of the galaxy properties based on their best estimates and the corresponding error bars and measure the scatter obtained per bin. The scatter associated with the properties is then added in quadrature to the Poisson statistics error bars and the scatter obtained from the flux density uncertainties. Given a population definition (e.g., range in dust mass), the number counts are estimated assuming this subsample as a new sample. We do not include any completeness correction based on the parameters estimated for the galaxies. In other words, we assume that the HUDF population is complete down to the levels we are testing.

When the sample is split by redshift, we note that in most of the flux density range the 1 mm selected population is dominated by galaxies in the redshift range of $z = 1$–3. For fainter sources we begin to see the rise of the $z < 1$ population. The main component of 1 mm galaxy population appears to be between $z = 1$–3, in agreement with the redshift distribution obtained for brighter sources (Simpson et al. 2014; Brisbin et al. 2017). It would appear that the population of 1 mm galaxies at $z > 4$ should be more important at brighter flux density ranges than the ones explored here; at the same time, the number density must be such that they are only detectable in large-area surveys. The redshift distribution of our sample has a median value that is in agreement with the predictions by Béthermin et al. (2015) based on the depth and wavelength of our observations. See details in Aravena et al. (2020).

The s+ample dust mass has a range between $M_{\rm dust} = 10^7$–$10^9 M_\odot$. The number counts show that the population with $M_{\rm dust} > 10^8 M_\odot$ is the only component for sources brighter than 0.2 mJy. For sources fainter than 0.1 mJy, the complete population is dominated by the $M_{\rm dust} < 10^8 M_\odot$ population.

The stellar mass range for our sample is $M_* = 10^9$–$10^{12} M_\odot$. All sources brighter than 0.1 mJy have stellar masses $M_* > 10^{10} M_\odot$. With the population of 1 mm galaxies with stellar mass between $M_* = 10^{10}$–$10^{11} M_\odot$ dominating the counts at all flux density ranges. More massive galaxies, with stellar masses $M_* > 10^{11} M_\odot$, are responsible for half of the counts in the flux density range 0.3–0.4 mJy, while the 1 mm galaxies $M_* = 10^9$–$10^{10} M_\odot$ only appear in the faint end of the counts with flux density values below 0.1 mJy.

Finally, when we split the number counts on SFR, we see how the brighter 1.2 mm sources are dominated by the population with SFR $> 100\ M_\odot\ {\rm yr}^{-1}$. In the range below 0.1 mJy, we see how the sources with $10\ M_\odot\ {\rm yr}^{-1} <$ SFR $< 100\ M_\odot\ {\rm yr}^{-1}$ dominate. The faint end of the population also has a small fraction of 1 mm galaxies with low SFR rates (SFR $< 10\ M_\odot\ {\rm yr}^{-1}$).

We find that the sources with $S_\nu < 0.1$ mJy, which correspond to the flattening of the number counts, are galaxies in the redshift range $1 < z < 2$, dust masses in the range $M_{\rm dust} = 10^7$–$10^8 M_\odot$, stellar masses in the range $M_* = 10^{10}$–$10^{11} M_\odot$, and SFR in the range $10\ M_\odot\ {\rm yr}^{-1} <$ SFR $< 100\ M_\odot\ {\rm yr}^{-1}$.

We remark that the predictions from Popping et al. (2020) seem to agree fairly well with the observations when split in redshift, dust mass, and SFR, but not so well when split in stellar mass. The latter disagreement could be explained by an overestimation of the stellar masses for some ASPECS galaxies because moving sources from the range $M_* = 10^{11}$–$10^{12} M_\odot$ into the lower range would alleviate the disagreement. In fact, we found that the agreement improved when different stellar mass ranges were used to split the number counts, indicating that the disagreement is partially caused by the ranges chosen for the comparison. It has been shown that MAGPHYS can overestimate the stellar mass of galaxies, while providing correct estimates of other properties when in the presence of active galactic nuclei (Hayward & Smith 2015). This effect could overestimate the stellar mass for some of our galaxies and produce the disagreement.

The comparison of the observations with the predictions from Popping et al. (2020) shows how these new results can be used to test different galaxy evolution models. The cumulative number counts for the different populations are presented in Tables 6–9.

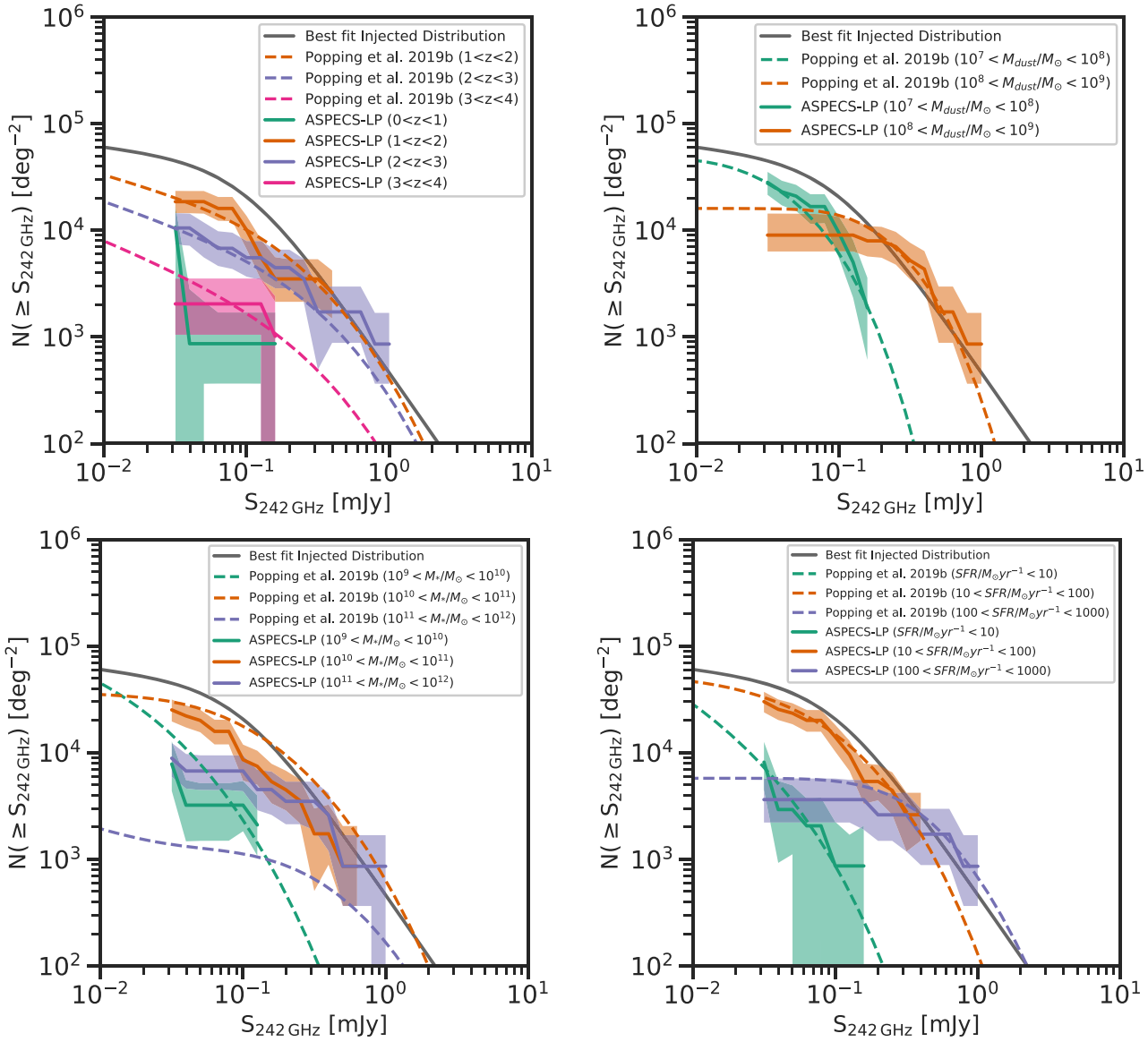

Figure 6. Number counts estimated using the detected sources with *HST* counterparts. We divided the sample based on redshift (top left), dust mass (top right), stellar mass (bottom left), and SFR (bottom right). The solid gray curve is the total cumulative number count fit shown in Figure 5. The dashed colored lines show the number count predictions by Popping et al. (2020).

5.3. Causes for the Flattening of the Number Counts

The flattening of the number counts is caused by the absence of a strongly increasing population of galaxies with flux density values lower than $S_\nu < 0.1$ mJy. We need to identify what types of galaxies could potentially be detected in this flux density range and how they compare with the detected sources. The companion paper, Popping et al. (2020), discusses the theoretical considerations in detail that predict the flattening of the counts and the properties of the galaxies producing it. According to these models (and in agreement with the results from the previous section), our deep observations are sensitive to galaxies with $M_* = 10^{10}$–$10^{11} M_\odot$ that are on the knee of the stellar and dust mass functions at $1 < z < 2$. Both mass functions flatten beyond the knee, so the number density of galaxies remains almost constant even when going deeper (i.e., observing less massive galaxies). This behavior is reflected as a flattening of number counts of sources fainter than $S_\nu < 0.1$ mJy. In addition to the number density effect, we are observing galaxies with $M_* \lesssim 10^{10} M_\odot$ that should have lower gas-phase metallicity than the more massive galaxies and therefore lower dust-to-gas ratios. The dust content, relative to the stellar and gas mass, associated with these galaxies should be lower than the one associated with more massive galaxies. The companion paper, Magnelli et al. (2020), used stacking to explore the dust content galaxies with different stellar mass ranges. They found that the comoving dust mass density associated with galaxies with $M_* \lesssim 10^{10} M_\odot$ at $1 < z < 3$ is fairly low, and that most of the dust mass is associated with more massive galaxies. Similar results are found by R. Bouwens et al. (2020, in preparation): they stacked the emission of all galaxies with $M_* < 10^{9.25} M_\odot$ at $1.5 < z < 10$ and found no dust continuum emission.

In summary, the flattening of the number counts at $S_\nu < 0.1$ mJy is produced by the lack of continuum emission in galaxies with $M_* \lesssim 10^{10} M_\odot$ at $1 < z < 2$. These galaxies are beyond the knee of the stellar and dust mass function, meaning that the number density of galaxies flattens. At the same time, these galaxies are within the stellar mass range where the gas-phase metallicity is low enough that the dust content associated with them also decreases, further limiting the number of dust continuum emission detections.

5.4. 1.2 mm EBL

To estimate how much of the 1.2 mm EBL is resolved by our observations, we fit a triple power-law (TPL) to the whole range of observed differential number counts presented in the bottom left panel of Figure 5. We need to use a TPL in order to account for the observed break of the number counts at ≈0.1 mJy (Table 2) and the break at ≈1.5 mJy already identified in wider and shallower observations (Franco et al. 2018; Stach et al. 2018). For the TPL we used the functional form

$$\frac{dN}{dS} = \left[\frac{1}{F_1(S)} + \frac{1}{F_2(S)}\right]^{-1}, \quad (6)$$

with

$$F_1(S) = \frac{N_0}{S_0}\left[\left(\frac{S}{S_0}\right)^{\alpha} + \left(\frac{S}{S_0}\right)^{\beta}\right]^{-1} \quad (7)$$

and

$$F_2(S) = F_1(S_1)\left(\frac{S}{S_1}\right)^{-\gamma}. \quad (8)$$

This TPL is a modification of the functional form presented in Wang et al. (2015). To fit the TPL, we used the ASPECS-LP counts in the range $S_\nu < 1$ mJy and other studies available for the brighter ones. We obtained a best fit of $S_1 = 1.7 \pm 0.2$ mJy and $\gamma = 5.2^{+0.3}_{-0.2}$ when the parameters for F_1 follow the 1σ range from the $P(D)$ analysis. We integrated the functional form of the differential number counts (TPL) to obtain the recovered EBL intensity (Franco et al. 2018). We integrated from 35 μJy to infinity and obtained an intensity of 6.3 ± 0.2 Jy deg^{-2}. We estimated the measurements we would obtain if we were to detect the entire continuum emission in the field. We integrated from zero to infinity and obtained an intensity of 6.8 ± 0.4 Jy deg^{-2}, which would be our estimate of the total EBL associated with 1 mm galaxies in the HUDF.

We compare these values estimated using the best fits of the $P(D)$ with the actual sources extracted in our observations. When we combine the total flux density of the sources presented in Table 1, we obtain 5.84 ± 0.12 Jy deg^{-2} (corrected for fidelity). In order to search for possible real continuum source detections that are skipped by our high-fidelity cut, we explored the fainter flux density regime. We selected all galaxies with $m_{\rm F160W} < 26.4$ in the HUDF and used the corrected Poissonian probability ($p \leqslant 0.05$) and the 1.2 mm S/N $\geqslant 3.0$ positions to select possible real associations (Downes et al. 1986; Casey et al. 2014). We complemented the sample by using the deep mid-infrared catalog from Elbaz et al. (2011). We selected all the *Spitzer*-MIPS and *Herschel*-PACS detected sources that show 1.2 mm emission with S/N $\geqslant 3.0$. Most of the sources selected by the mid-infrared prior detections are also selected by their *HST* detection. The number of source candidates with S/N $\geqslant 3.0$ and not selected in the main sample of detection is ≈70 (including sources in the natural and tapered images). The cross match was made in the same way as for the counterpart search, where the allowed offset is given by the corresponding synthesized beam of the detection (see Section 4). In Table 5 we present the list of 26 1 mm galaxies selected using this method. More details about this complementary sample are presented in Aravena et al. (2020). When we combine the flux density values of the sources, we obtain an additional value of 0.93 ± 0.07 Jy deg^{-2}. Combined with the high-fidelity sample, we thus obtain a total recovered 1.2 mm intensity of 6.77 ± 0.14 Jy deg^{-2}. This value is in good agreement with the intensity that we should recover in the whole field based on the best-fit differential number counts integrating from 35 μJy to infinity. In conclusion, by integrating our different number counts and on the secure sources, we recover ∼93% of the our total estimate for the EBL associated with 1 mm galaxies in the HUDF. The recovered emission is closer to ∼100% when we include the faint sample.

Using our best-fit differential number counts, we estimate that by going deeper in the same field, to an rms value ≈5 μJy beam^{-1} (340 hr total time in similar weather conditions as ASPECS-LP), we would recover ≈99% of our 1.2 mm EBL total estimate. These same observations would only return about 5 additional sources to the 47 sources that are already discovered (main and secondary samples combined).

Our total estimate for 1.2 mm EBL is lower than previous estimates. Our estimated 3σ upper limit of <8 Jy deg^{-2} for the HUDF contradicts the values expected at 242 GHz estimated from Planck observations of 14–24 Jy deg^{-2} (Planck Collaboration et al. 2014; Odegard et al. 2019). It is important to mention that these estimates are obtained after subtracting the CMB and Galactic dust emission from the observations. This process involved several assumptions and uncertainties, and is not as direct as the count of sources presented here. Our 3σ upper limit is closer to but still lower than previous estimates of 8–10 Jy deg^{-2} (Aravena et al. 2016; Oteo et al. 2016) and to the values of 10–13 Jy deg^{-2} obtained from modeling the CIB at multiple wavelengths (Béthermin et al. 2012; Khaire & Srianand 2019). In a companion paper, Popping et al. (2020) estimate the effects of cosmic variance on the number count measurements. For the wavelength and size of the ASPECS-LP 1.2 mm image they estimate a 2σ scatter of a factor of 1.5. Such low values of cosmic variance are expected because the negative K-correction at 1.2 mm allows us to sample a large volume ($z \approx 1$–8) despite the small observed area (Casey et al. 2014). This shows that cosmic variance is not enough to reconcile our estimate of the total 1.2 mm EBL with previous studies.

5.5. Confusion Noise

In this section we determine the presence of confusion noise in our observations. As stated by several authors (Condon 1974; Scheuer 1974), the confusion noise is a source of noise that is

Table 5
Continuum Source Candidates in ASPECS-LP 1 mm Continuum Image Selected by their *HST* Counterpart

ID ASPECS-LP.1 mm.Faint.	R.A.	Decl.	S/N	Fidelity	PBC	$S_{1.2\,\mathrm{mm}}$ (μJy)	*HST* prior	Mid-IR prior
(1)	(2)	(3)	(4)	(5)	(6)	(7)	(8)	(9)
C01	03:32:34.66	−27:47:21.20	3.9	0.91	0.68	55.6 ± 13.7	1	1
C02	03:32:35.74	−27:46:39.60	3.8	0.9	0.87	41.7 ± 10.7	1	1
C03	03:32:41.32	−27:47:06.60	3.7	0.91	0.95	38.0 ± 9.8	1	0
C04	03:32:41.47	−27:47:29.20	3.7	0.92	0.59	60.4 ± 15.8	1	0
C05	03:32:37.51	−27:47:56.60	3.6	0.9	0.49	70.4 ± 18.9	1	0
C06	03:32:41.63	−27:46:25.80	3.6	0.9	0.45	76.2 ± 20.5	1	0
C07	03:32:40.01	−27:47:51.20	3.5	0.83	0.66	51.3 ± 14.0	1	0
C08	03:32:35.85	−27:47:18.60	3.5	0.9	0.98	34.6 ± 9.5	1	1
C09	03:32:38.56	−27:47:30.60	3.4	0.9	1.0	33.3 ± 9.3	1	0
C10	03:32:38.62	−27:47:34.40	3.4	0.85	1.0	32.7 ± 9.3	1	0
C11	03:32:36.66	−27:46:31.20	3.3	0.87	0.93	34.7 ± 10.0	1	1
C12	03:32:37.17	−27:46:26.20	3.3	0.85	0.95	33.4 ± 9.8	1	0
C13	03:32:37.85	−27:47:51.80	3.2	0.85	0.79	39.5 ± 11.7	1	0
C14	03:32:35.36	−27:47:17.00	3.2	0.81	0.95	32.1 ± 9.8	1	0
C15	03:32:38.36	−27:46:00.20	3.1	0.81	0.69	44.1 ± 13.5	1	0
C16	03:32:35.79	−27:46:55.40	3.1	0.82	0.99	30.6 ± 9.4	1	1
C17	03:32:38.56	−27:46:31.00	3.0	0.8	0.97	34.8 ± 9.6	1	0
C18	03:32:37.32	−27:45:57.80	3.0	0.8	0.47	62.5 ± 19.9	1	1
C19	03:32:38.98	−27:46:31.00	3.8	0.8	0.96	43.9 ± 11.7	1	1
C20	03:32:39.89	−27:46:07.40	3.6	0.82	0.47	85.8 ± 23.8	1	1
C21	03:32:41.35	−27:46:52.00	3.5	0.84	0.95	54.0 ± 15.2	1	1
C22	03:32:37.60	−27:47:40.60	3.4	0.85	0.95	39.7 ± 11.9	1	0
C23	03:32:42.37	−27:46:57.80	3.0	0.81	0.89	38.8 ± 12.7	1	1
C24	03:32:36.86	−27:46:35.00	3.0	0.82	0.96	35.9 ± 11.8	1	0
C25	03:32:41.80	−27:47:39.00	3.0	0.83	0.21	165.2 ± 54.2	1	1
C26	03:32:38.09	−27:46:14.14	3.0	0.50	0.94	39.5 ± 12.0	0	1

Note. (1) Identification for continuum source candidates discovered in ASPECS-LP 1.2 mm continuum image. (2) R.A. (J2000). (3) decl. (J2000). (4) S/N value obtained by LineSeeker assuming an unresolved source. (5) Fidelity estimate using negative detection and Poisson statistics. (6) Mosaic primary beam correction. (7) Integrated flux density at 1.2 mm obtained after removing the channels with bright emission lines when necessary. (8) If the source is detected based on the *HST* prior. (9) If the source is detected based on the mid-infrared prior (*Spitzer*-MIPS and *Herschel*-PACS).

not produced by the instruments or the atmosphere. It is the noise produced by the background of faint unresolved sources that follow a steep distribution (Hogg 2001). The confusion noise is usually estimated as

$$\sigma_c = \sqrt{\sigma_o^2 - \sigma_n^2}, \tag{9}$$

with σ_o the observed noise in the image and σ_n the intrinsic noise of the observations (instrumental + atmospheric; Condon et al. 2012). In our case, we have an observed value of $\sigma_o = 9.3$ μJy beam^{-1} (see Section 2) and an estimated $\sigma_n = 9.2$ μJy beam^{-1} (see Section 3.3). From these values we can estimate a confusion noise of $\sigma_o = 1.4$ μJy beam^{-1}. When we remove the 35 sources that were discovered as part of this work by fitting a 2D Gaussian emission and measure the rms of the residual image, the value is close to $\sigma_o = 9.2$ μJy beam^{-1}, which would indicate that in fact we are not observing confusion noise but some residuals/sidelobs from real emission that is not properly cleaned. The lack of confusion noise in our observations is in line with the flattening of the number counts and the small synthesized beam (see Section 2).

6. Conclusion

In this paper we presented the analysis of the deep 1.2 mm continuum image of the HUDF obtained as part of the ASPECS-LP. The image covered an area of 4.2 (2.9) arcmin^2 within the 10% (50%) response of the mosaic primary beam and to a one-sigma level of $\sigma = 9.3$ μJy beam^{-1}. With our source extraction methods we recovered 35 significant continuum sources, out of which 32 have clear NIR counterpart galaxies. We estimated the number counts using two independent methods, one that directly used the detected sources, corrected for fidelity and completeness. The second method was the $P(D)$ analysis.

For the $P(D)$ analysis, we use two novel and independent methods to obtain a reliable representation of the observational noise within our image. We made use of jackknife resampling in the *uv*-plane and in the channel space to obtain continuum noise-reference images. The comparison between the different methods showed that the intrinsic noise level of our images is of $\sigma = 9.2$ μJy beam^{-1}. The $P(D)$ analysis was performed by injecting sources to the noise image following different intrinsic differential number counts. The best-fit number counts were found by comparing the pixel distribution of the resulting image with the pixel distribution of the observed dirty image. We find that the $P(D)$ analysis number counts are in good agreement with the number counts estimated using the individually detected sources. Importantly, both analysis showed that the number counts flatten at $S_\nu \lesssim 0.1$ mJy.

We compared our number count results with other studies and models. We found a good agreement of our results with

Table 6
ASPECS-LP 1 mm Continuum Number Counts in Redshift Ranges

S_ν range ($\times 10^{-3}$ mJy) (1)	$\log S_\nu$ (mJy) (2)	$N(S_\nu)$ (3)	$N(\geqslant S_\nu)$ ($\deg^{-2}$) (4)	δN_- ($\deg^{-2}$) (5)	δN^+ ($\deg^{-2}$) (6)
$0 < z < 1$					
31.6–39.8	−1.45	3	10,700	4800	6300
39.8–50.1	−1.35	0	900	1700	1900
50.1–63.1	−1.25	0	860	500	1300
63.1–79.4	−1.15	0	860	500	830
79.4–100.0	−1.05	0	860	500	830
100.0–125.9	−0.95	0	860	500	830
125.9–158.5	−0.85	0	860	500	830
158.5–199.5	−0.75	1	860	960	830
199.5–251.2	−0.65	0	<1600	⋯	⋯
$1 < z < 2$					
31.6–39.8	−1.45	0	18,600	4100	4900
39.8–50.1	−1.35	0	18,600	4100	4800
50.1–63.1	−1.25	2	18,600	4200	4800
63.1–79.4	−1.15	0	16,100	3800	4500
79.4–100.0	−1.05	5	16,100	3900	4500
100.0–125.9	−0.95	4	10,100	3400	3600
125.9–158.5	−0.85	2	5600	2200	2700
158.5–199.5	−0.75	0	3500	1400	2100
199.5–251.2	−0.65	0	3500	1400	1900
251.2–316.2	−0.55	0	3500	1400	1900
316.2–398.1	−0.45	1	3500	1600	1900
398.1–501.2	−0.35	3	2600	1100	1600
501.2–631.0	−0.25	0	<1600	⋯	⋯
$2 < z < 3$					
31.6–39.8	−1.45	0	10,500	3200	4000
39.8–50.1	−1.35	1	10,500	3300	3800
50.1–63.1	−1.25	1	8500	2900	3400
63.1–79.4	−1.15	0	6800	2200	3000
79.4–100.0	−1.05	1	6800	2400	2700
100.0–125.9	−0.95	0	5500	1900	2400
125.9–158.5	−0.85	1	5500	2100	2400
158.5–199.5	−0.75	0	4500	1600	2100
199.5–251.2	−0.65	1	4500	1600	2100
251.2–316.2	−0.55	2	3500	1400	1900
316.2–398.1	−0.45	0	1700	1200	1300
398.1–501.2	−0.35	0	1720	840	1250
501.2–631.0	−0.25	0	1720	840	1250
631.0–794.3	−0.15	1	1720	840	1250
794.3–1000.0	−0.05	0	860	490	820
1000.0–1258.9	0.05	1	860	490	820
1258.9–1584.9	0.15	0	<1600	⋯	⋯
$3 < z < 4$					
31.6–39.8	−1.45	0	2040	1000	1490
39.8–50.1	−1.35	0	2040	1000	1490
50.1–63.1	−1.25	0	2040	1000	1490
63.1–79.4	−1.15	0	2040	1000	1490
79.4–100.0	−1.05	0	2040	1000	1490
100.0–125.9	−0.95	0	2040	1000	1490
125.9–158.5	−0.85	1	2040	1000	1490
158.5–199.5	−0.75	1	1000	1200	1400
199.5–251.2	−0.65	0	<1600	⋯	⋯

Note. (1) Flux density bin. (2) Flux density bin center. (3) Number of sources per bin (before fidelity and completeness correction). In the case of no sources, an upper limit of <1.83 is used. (4) Cumulative number count of sources per square degree. In the case of no sources, a 1σ upper limit is used. (5) Lower uncertainty in the number counts. (6) Upper uncertainty in the number counts.

other studies at $S_\nu > 0.1$ mJy but not for the fainter sources. The only other number count estimates that show a flattening at $S_\nu < 0.1$ mJy correspond to the ALMA observations of the Hubble Frontier Fields. Our number count results are in good agreement with the shapes of cumulative number counts predicted using models of galaxy evolution. With the detected sources we recovered an intensity of 6.3 ± 0.2 Jy $\deg^{-2}$, which is ∼94% of our total estimate of the EBL of 6.8 ± 0.4 Jy $\deg^{-2}$ for the HUDF. We predicted that doubling the integration time of our observations would only add about five additional sources to those that are detected with high fidelity and those selected by their counterparts (discussed in Aravena et al. 2020).

Finally, we presented the number counts for different galaxy populations, split according to redshift, dust mass, stellar mass, and SFR. These resolved number counts offer a unique opportunity to test our understanding of the evolution of galaxies across time. We found that the sources with $S_\nu < 0.1$ mJy (where we detect the flattening of the counts) are dominated by 1 mm galaxies in the redshift range $1 < z < 2$, dust masses in the range $M_{\rm dust} = 10^7$–$10^8 M_\odot$, stellar masses in the range $M_* = 10^{10}$–$10^{11} M_\odot$, and an SFR in the range $10\ M_\odot\ {\rm yr}^{-1} < {\rm SFR} < 100\ M_\odot\ {\rm yr}^{-1}$.

We thank the referee for helpful comments that improved this paper.

This paper makes use of the ALMA data ADS/JAO. ALMA#2016.1.00324.L. ALMA is a partnership of ESO (representing its member states), NSF (USA) and NINS (Japan), together with NRC (Canada), NSC and ASIAA (Taiwan), and KASI (Republic of Korea), in cooperation with the Republic of Chile. The Joint ALMA Observatory is operated by ESO, AUI/NRAO and NAOJ. The National Radio Astronomy Observatory is a facility of the National Science Foundation operated under cooperative agreement by Associated Universities, Inc. "Este trabajo contó con el apoyo de CONICYT + Programa de Astronomía+ Fondo CHINA-CONICYT CAS16026." M.N. and F.W. acknowledge support from ERC Advanced grant 740246 (Cosmic Gas). D.R. acknowledges support from the National Science Foundation under grant no. AST-1614213 and from the Alexander von Humboldt Foundation through a Humboldt Research Fellowship for Experienced Researchers. R.J.A. was supported by FONDECYT grant number 1191124. I.R.S. acknowledges support from STFC (ST/P000541/1). B.M. acknowledge support from the Collaborative Research Centre 956, subproject A1, funded by the Deutsche Forschungsgemeinschaft (DFG)—project ID 184018867. We acknowledge support from CONICYT grants CATA-Basal AFB-170002 (FEB); FONDECYT Regular 1190818 (FEB); Chile's Ministry of Economy, Development, and Tourism's Millennium Science. Initiative through grant IC120009, awarded to The Millennium Institute of Astrophysics, MAS (FEB). Este trabajo cont ó con el apoyo de CONICYT + PCI + INSTITUTO MAX PLANCK DE ASTRONOMIA MPG190030 (M.A.).

Facility: ALMA.

Software: Astropy (Astropy Collaboration et al. 2013), LineSeeker.

Appendix

Tables 7–9 show the cumulative number counts for the different populations.

Table 7
ASPECS-LP 1 mm Continuum Number Counts in Dust Mass Ranges

S_ν range ($\times 10^{-3}$ mJy) (1)	$\log S_\nu$ (mJy) (2)	$N(S_\nu)$ (3)	$N(\geqslant S_\nu)$ (deg^{-2}) (4)	δN_- (deg^{-2}) (5)	δN^+ (deg^{-2}) (6)
$10^7 < M_{\rm dust}/M_\odot < 10^8$					
31.6–39.8	−1.45	2	28,200	6700	7200
39.8–50.1	−1.35	1	23,000	5800	6200
50.1–63.1	−1.25	3	21,000	5700	5800
63.1–79.4	−1.15	0	16,700	5300	5100
79.4–100.0	−1.05	6	16,700	5100	5100
100.0–125.9	−0.95	4	9500	4000	4000
125.9–158.5	−0.85	3	5000	2700	3100
158.5–199.5	−0.75	2	1900	1300	1700
199.5–251.2	−0.65	0	<1600	…	…
$10^8 < M_{\rm dust}/M_\odot < 10^9$					
31.6–39.8	−1.45	0	9000	2700	5400
39.8–50.1	−1.35	0	9000	2700	5300
50.1–63.1	−1.25	0	9000	2700	5300
63.1–79.4	−1.15	0	9000	2700	5300
79.4–100.0	−1.05	0	9000	2700	5200
100.0–125.9	−0.95	0	9000	2700	4400
125.9–158.5	−0.85	1	9000	2700	3600
158.5–199.5	−0.75	0	8000	2300	3000
199.5–251.2	−0.65	1	8000	2400	2800
251.2–316.2	−0.55	2	7000	2300	2600
316.2–398.1	−0.45	1	5200	1800	2400
398.1–501.2	−0.35	3	4300	1600	2100
501.2–631.0	−0.25	0	1720	840	1250
631.0–794.3	−0.15	1	1720	840	1250
794.3–1000.0	−0.05	0	860	490	820
1000.0–1258.9	0.05	1	860	490	820
1258.9–1584.9	0.15	0	<1600	…	…

Note. (1) Flux density bin. (2) Flux density bin center. (3) Number of sources per bin (before fidelity and completeness correction). In the case of no sources, an upper limit of <1.83 is used. (4) Cumulative number count of sources per square degree. In the case of no sources, a 1σ upper limit is used. (5) Lower uncertainty in the number counts. (6) Upper uncertainty in the number counts.

Table 8
ASPECS-LP 1 mm Continuum Number Counts in Stellar Mass Ranges

S_ν range ($\times 10^{-3}$ mJy) (1)	$\log S_\nu$ (mJy) (2)	$N(S_\nu)$ (3)	$N(\geqslant S_\nu)$ (deg^{-2}) (4)	δN_- (deg^{-2}) (5)	δN^+ (deg^{-2}) (6)
$10^9 < M_*/M_\odot < 10^{10}$					
31.6–39.8	−1.45	1	7800	3400	4900
39.8–50.1	−1.35	0	3200	1700	2300
50.1–63.1	−1.25	0	3200	1700	2000
63.1–79.4	−1.15	0	3200	1700	2000
79.4–100.0	−1.05	0	3200	1700	2000
100.0–125.9	−0.95	1	3200	1400	2200
125.9–158.5	−0.85	2	2100	1000	1900
158.5–199.5	−0.75	0	<1600	…	…
$10^{10} < M_*/M_\odot < 10^{11}$					
31.6–39.8	−1.45	1	25,200	5600	6300
39.8–50.1	−1.35	1	22,100	4900	5600
50.1–63.1	−1.25	3	20,000	4500	5200
63.1–79.4	−1.15	0	15,800	3900	4600
79.4–100.0	−1.05	6	15,800	3900	4500
100.0–125.9	−0.95	1	8600	3100	3300
125.9–158.5	−0.85	2	7400	2500	3000
158.5–199.5	−0.75	1	5300	2000	2500
199.5–251.2	−0.65	1	4500	1600	2300
251.2–316.2	−0.55	2	3500	1400	2100
316.2–398.1	−0.45	0	1700	1200	1300
398.1–501.2	−0.35	1	1730	840	1520
501.2–631.0	−0.25	0	860	490	1190
631.0–794.3	−0.15	1	860	490	1190
794.3–1000.0	−0.05	0	<1600	…	…
$10^{11} < M_*/M_\odot < 10^{12}$					
31.6–39.8	−1.45	1	8900	2900	3500
39.8–50.1	−1.35	0	6700	2100	3000
50.1–63.1	−1.25	0	6700	2300	2700
63.1–79.4	−1.15	0	6700	2300	2700
79.4–100.0	−1.05	0	6700	2300	2700
100.0–125.9	−0.95	2	6700	2400	2700
125.9–158.5	−0.85	0	4500	1600	2400
158.5–199.5	−0.75	1	4500	1900	2100
199.5–251.2	−0.65	0	3500	1400	1900
251.2–316.2	−0.55	0	3500	1400	1900
316.2–398.1	−0.45	1	3500	1600	1900
398.1–501.2	−0.35	2	2600	1400	1600
501.2–631.0	−0.25	0	860	490	820
631.0–794.3	−0.15	0	860	490	820
794.3–1000.0	−0.05	0	860	490	820
1000.0–1258.9	0.05	1	860	990	820
1258.9–1584.9	0.15	0	<1600	…	…

Note. (1) Flux density bin. (2) Flux density bin center. (3) Number of sources per bin (before fidelity and completeness correction). In the case of no sources, an upper limit of <1.83 is used. (4) Cumulative number count of sources per square degree. In the case of no sources, a 1σ upper limit is used. (5) Lower uncertainty in the number counts. (6) Upper uncertainty in the number counts.

Table 9
ASPECS-LP 1 mm Continuum Number Counts in Star Formation Rate Ranges

S_ν range ($\times 10^{-3}$ mJy) (1)	$\log S_\nu$ (mJy) (2)	$N(S_\nu)$ (3)	$N(\geqslant S_\nu)$ (deg^{-2}) (4)	δN_- (deg^{-2}) (5)	δN^+ (deg^{-2}) (6)
SFR$/M_\odot$ yr^{-1} < 10					
31.6–39.8	−1.45	2	8100	3700	4500
39.8–50.1	−1.35	0	2900	2000	2500
50.1–63.1	−1.25	1	2900	1800	2000
63.1–79.4	−1.15	0	2100	2200	1700
79.4–100.0	−1.05	1	2100	1600	1700
100.0–125.9	−0.95	0	860	990	1380
125.9–158.5	−0.85	0	860	960	830
158.5–199.5	−0.75	1	860	500	1190
199.5–251.2	−0.65	0	<1600	…	…
10 < SFR$/M_\odot$ yr^{-1} < 100					
31.6–39.8	−1.45	1	30,100	6200	7100
39.8–50.1	−1.35	1	25,500	5300	6000
50.1–63.1	−1.25	2	23,400	4900	5600
63.1–79.4	−1.15	0	20,100	4400	5000
79.4–100.0	−1.05	5	20,100	4400	5000
100.0–125.9	−0.95	4	14,000	3800	4200

Table 9
(Continued)

S_ν range ($\times 10^{-3}$ mJy) (1)	$\log S_\nu$ (mJy) (2)	$N(S_\nu)$ (3)	$N(\geqslant S_\nu)$ (deg^{-2}) (4)	δN_- (deg^{-2}) (5)	δN^+ (deg^{-2}) (6)
125.9–158.5	−0.85	4	9600	2800	3400
158.5–199.5	−0.75	0	5400	2100	2500
199.5–251.2	−0.65	1	5400	1800	2300
251.2–316.2	−0.55	2	4400	1800	2100
316.2–398.1	−0.45	0	2600	1400	1600
398.1–501.2	−0.35	3	2600	1100	1600
501.2–631.0	−0.25	0	<1600	...	...
$100 < SFR/M_\odot$ yr^{-1}1000					
31.6–39.8	−1.45	0	3600	1400	2100
39.8–50.1	−1.35	0	3600	1400	2100
50.1–63.1	−1.25	0	3600	1400	2100
63.1–79.4	−1.15	0	3600	1400	2100
79.4–100.0	−1.05	0	3600	1400	2100
100.0–125.9	−0.95	0	3600	1400	2100
125.9–158.5	−0.85	0	3600	1400	1900
158.5–199.5	−0.75	1	3600	1700	1900
199.5–251.2	−0.65	0	2600	1100	1600
251.2–316.2	−0.55	0	2600	1100	1600
316.2–398.1	−0.45	1	2600	1400	1600
398.1–501.2	−0.35	0	1720	840	1250
501.2–631.0	−0.25	0	1720	840	1250
631.0–794.3	−0.15	1	1720	840	1250
794.3–1000.0	−0.05	0	860	490	820
1000.0–1258.9	0.05	1	860	490	820
1258.9–1584.9	0.15	0	<1600	...	...

Note. (1) Flux density bin. (2) Flux density bin center. (3) Number of sources per bin (before fidelity and completeness correction). In the case of no sources, an upper limit of <1.83 is used. (4) Cumulative number count of sources per square degree. In the case of no sources, a 1σ upper limit is used. (5) Lower uncertainty in the number counts. (6) Upper uncertainty in the number counts.

ORCID iDs

Jorge González-López https://orcid.org/0000-0003-3926-1411
Mladen Novak https://orcid.org/0000-0001-8695-825X
Roberto Decarli https://orcid.org/0000-0002-2662-8803
Fabian Walter https://orcid.org/0000-0003-4793-7880
Manuel Aravena https://orcid.org/0000-0002-6290-3198
Chris Carilli https://orcid.org/0000-0001-6647-3861
Leindert Boogaard https://orcid.org/0000-0002-3952-8588
Gergö Popping https://orcid.org/0000-0003-1151-4659
Axel Weiss https://orcid.org/0000-0003-4678-3939
Roberto J. Assef https://orcid.org/0000-0002-9508-3667
Franz Erik Bauer https://orcid.org/0000-0002-8686-8737
Rychard Bouwens https://orcid.org/0000-0002-4989-2471
Paulo C. Cortes https://orcid.org/0000-0002-3583-780X
Emanuele Daddi https://orcid.org/0000-0002-3331-9590
Rob Ivison https://orcid.org/0000-0001-5118-1313
Benjamin Magnelli https://orcid.org/0000-0002-6777-6490
Dominik Riechers https://orcid.org/0000-0001-9585-1462
Ian Smail https://orcid.org/0000-0003-3037-257X

References

ALMA Partnership, Brogan, C. L., Pérez, L. M., et al. 2015, ApJL, 808, L3
Astropy Collaboration, Robitaille, T. P., Tollerud, E. J., et al. 2013, A&A, 558, A33
Aravena, M., Boogaard, L., González López, J. I., et al. 2020, ApJ, in press
Aravena, M., Decarli, R., Gónzalez-López, J., et al. 2019, arXiv:1903.09162
Aravena, M., Decarli, R., Walter, F., et al. 2016, ApJ, 833, 68
Barger, A. J., Cowie, L. L., Sanders, D. B., et al. 1998, Natur, 394, 248
Beckwith, S. V. W., Stiavelli, M., Koekemoer, A. M., et al. 2006, AJ, 132, 1729
Béthermin, M., Daddi, E., Magdis, G., et al. 2012, ApJL, 757, L23
Béthermin, M., De Breuck, C., Sargent, M., & Daddi, E. 2015, A&A, 576, L9
Béthermin, M., Wu, H.-Y., Lagache, G., et al. 2017, A&A, 607, A89
Blain, A. W., Smail, I., Ivison, R. J., et al. 2002, PhR, 369, 111
Boogaard, L. A., Decarli, R., González-López, J., et al. 2019, arXiv:1903.09167
Bouwens, R. J., Oesch, P. A., Illingworth, G. D., Ellis, R. S., & Stefanon, M. 2017, ApJ, 843, 129
Brisbin, D., Miettinen, O., Aravena, M., et al. 2017, A&A, 608, A15
Carniani, S., Maiolino, R., De Zotti, G., et al. 2015, A&A, 584, A78
Casey, C. M., Narayanan, D., & Cooray, A. 2014, PhR, 541, 45
Cash, W. 1979, ApJ, 228, 939
Chabrier, G. 2003, PASP, 115, 763
Chapin, E. L., Pope, A., Scott, D., et al. 2009, MNRAS, 398, 1793
Clements, D. L., Dunne, L., & Eales, S. 2010, MNRAS, 403, 274
Condon, J. J. 1974, ApJ, 188, 279
Condon, J. J., Cotton, W. D., Fomalont, E. B., et al. 2012, ApJ, 758, 23
da Cunha, E., Charlot, S., & Elbaz, D. 2008, MNRAS, 388, 1595
da Cunha, E., Groves, B., Walter, F., et al. 2013, ApJ, 766, 13
da Cunha, E., Walter, F., Decarli, R., et al. 2013, ApJ, 765, 9
da Cunha, E., Walter, F., Smail, I. R., et al. 2015, ApJ, 806, 110
Decarli, R., Walter, F., Gónzalez-López, J., et al. 2019, arXiv:1903.09164
Downes, A. J. B., Peacock, J. A., Savage, A., & Carrie, D. R. 1986, MNRAS, 218, 31
Draine, B. T. 2011, in Physics of the Interstellar and Intergalactic Medium, ed. B. T. Draine (Princeton, NJ: Princeton Univ. Press)
Dunlop, J. S., McLure, R. J., Biggs, A. D., et al. 2017, MNRAS, 466, 861
Dunne, L., & Eales, S. A. 2001, MNRAS, 327, 697
Eales, S., Lilly, S., Gear, W., et al. 1999, ApJ, 515, 518
Elbaz, D., Dickinson, M., Hwang, H. S., et al. 2011, A&A, 533, A119
Ester, M., Kriegel, H.-P., Sander, J., & Xu, X. 1996, in Proc. 2nd Int. Conf. Knowledge Discovery and Data Mining (Cambridge, MA: AAAI Press), 226, https://www.aaai.org/Papers/KDD/1996/KDD96-037.pdf
Fixsen, D. J., Dwek, E., Mather, J. C., Bennett, C. L., & Shafer, R. A. 1998, ApJ, 508, 123
Franco, M., Elbaz, D., Béthermin, M., et al. 2018, A&A, 620, A152
Fujimoto, S., Ouchi, M., Ono, Y., et al. 2016, ApJS, 222, 1
González-López, J., Bauer, F. E., Romero-Cañizales, C., et al. 2017, A&A, 597, A41
González-López, J., Decarli, R., Pavesi, R., et al. 2019, arXiv:1903.09161
Hashimoto, T., Inoue, A. K., Mawatari, K., et al. 2019, PASJ, 71, 71
Hatsukade, B., Kohno, K., Umehata, H., et al. 2016, PASJ, 68, 36
Hatsukade, B., Kohno, K., Yamaguchi, Y., et al. 2018, PASJ, 70, 105
Hatsukade, B., Ohta, K., Seko, A., Yabe, K., & Akiyama, M. 2013, ApJL, 769, L27
Hauser, M. G., Arendt, R. G., Kelsall, T., et al. 1998, ApJ, 508, 25
Hauser, M. G., & Dwek, E. 2001, ARA&A, 39, 249
Hayward, C. C., & Smith, D. J. B. 2015, MNRAS, 446, 1512
Hodge, J. A., Karim, A., Smail, I., et al. 2013, ApJ, 768, 91
Hodge, J. A., Swinbank, A. M., Simpson, J. M., et al. 2016, ApJ, 833, 103
Hogg, D. W. 2001, AJ, 121, 1207
Hughes, D. H., Serjeant, S., Dunlop, J., et al. 1998, Natur, 394, 241
Illingworth, G. D., Magee, D., Oesch, P. A., et al. 2013, ApJS, 209, 6
Iono, D., Yun, M. S., Aretxaga, I., et al. 2016, ApJL, 829, L10
Karim, A., Swinbank, A. M., Hodge, J. A., et al. 2013, MNRAS, 432, 2
Khaire, V., & Srianand, R. 2019, MNRAS, 484, 4174
Klypin, A., Yepes, G., Gottlöber, S., Prada, F., & Heß, S. 2016, MNRAS, 457, 4340
Klypin, A. A., Trujillo-Gomez, S., & Primack, J. 2011, ApJ, 740, 102
Lagos, C., del, P., Robotham, A. S. G., Trayford, J. W., et al. 2019, MNRAS, 489, 4196
Laporte, N., Ellis, R. S., Boone, F., et al. 2017, ApJL, 837, L21
Lotz, J. M., Koekemoer, A., Coe, D., et al. 2017, ApJ, 837, 97
Madau, P., & Dickinson, M. 2014, ARA&A, 52, 415
Magdis, G. E., Daddi, E., Béthermin, M., et al. 2012, ApJ, 760, 6
Magnelli, B., Boogaard, L., Decarli, R., et al. 2020, ApJ, 892, 66
Magnelli, B., Lutz, D., Saintonge, A., et al. 2014, A&A, 561, A86
McMullin, J. P., Waters, B., Schiebel, D., Young, W., & Golap, K. 2007, in ASP Conf. Ser. 376, Astronomical Data Analysis Software and Systems XVI, ed. R. A. Shaw, F. Hill, & D. J. Ball (San Francisco, CA: ASP), 127

Meneghetti, M., Natarajan, P., Coe, D., et al. 2017, MNRAS, 472, 3177
Muñoz Arancibia, A. M., González-López, J., Ibar, E., et al. 2018, A&A, 620, A125
Muñoz Arancibia, A. M., Navarrete, F. P., Padilla, N. D., et al. 2015, MNRAS, 446, 2291
Odegard, N., Weiland, J. L., Fixsen, D. J., et al. 2019, ApJ, 877, 40
Ono, Y., Ouchi, M., Kurono, Y., & Momose, R. 2014, ApJ, 795, 5
Oteo, I., Zwaan, M. A., Ivison, R. J., Smail, I., & Biggs, A. D. 2016, ApJ, 822, 36
Perera, T. A., Chapin, E. L., Austermann, J. E., et al. 2008, MNRAS, 391, 1227
Planck Collaboration, Abergel, A., Ade, P. A. R., et al. 2011a, A&A, 536, A25
Planck Collaboration, Ade, P. A. R., Aghanim, N., et al. 2014, A&A, 571, A30
Planck Collaboration, Ade, P. A. R., Aghanim, N., et al. 2011b, A&A, 536, A18
Popping, G., Pillepich, A., Somerville, R. S., et al. 2019, arXiv:1903.09158
Popping, G., Walter, F., Behroozi, P., et al. 2020, ApJ, 891, 135
Priewe, J., Williams, L. L. R., Liesenborgs, J., Coe, D., & Rodney, S. A. 2017, MNRAS, 465, 1030
Puget, J.-L., Abergel, A., Bernard, J.-P., et al. 1996, A&A, 308, L5
Sargent, M. T., Béthermin, M., Daddi, E., & Elbaz, D. 2012, ApJL, 747, L31
Scheuer, P. A. G. 1974, MNRAS, 166, 329
Schreiber, C., Elbaz, D., Pannella, M., et al. 2017, A&A, 602, A96
Schreiber, C., Elbaz, D., Pannella, M., et al. 2018, A&A, 609, A30
Scott, K. S., Austermann, J. E., Perera, T. A., et al. 2008, MNRAS, 385, 2225
Scott, S. E., Fox, M. J., Dunlop, J. S., et al. 2002, MNRAS, 331, 817
Simpson, J. M., Smail, I., Swinbank, A. M., et al. 2015, ApJ, 807, 128
Simpson, J. M., Swinbank, A. M., Smail, I., et al. 2014, ApJ, 788, 125
Smail, I., Ivison, R. J., & Blain, A. W. 1997, ApJL, 490, L5
Stach, S. M., Smail, I., Swinbank, A. M., et al. 2018, ApJ, 860, 161
Tadaki, K., Iono, D., Yun, M. S., et al. 2018, Natur, 560, 613
Umehata, H., Tamura, Y., Kohno, K., et al. 2017, ApJ, 835, 98
Walter, F., Decarli, R., Aravena, M., et al. 2016, ApJ, 833, 67
Walter, F., Decarli, R., Carilli, C., et al. 2012, Natur, 486, 233
Wang, T., Schreiber, C., Elbaz, D., et al. 2019, Natur, 572, 211
Wang, X.-G., Zhang, B., Liang, E.-W., et al. 2015, ApJS, 219, 9
Watson, D., Christensen, L., Knudsen, K. K., et al. 2015, Natur, 519, 327
Weiß, A., Kovács, A., Coppin, K., et al. 2009, ApJ, 707, 1201
Whitaker, K. E., Pope, A., Cybulski, R., et al. 2017, ApJ, 850, 208
Williams, C. C., Labbe, I., Spilker, J., et al. 2019, ApJ, 884, 154